Reexamination of the electronic phase diagram of doped NiS_2: Electronic, magnetic, and structural inhomogeneity across the Mott insulator-metal transition

Yu Tao,[1] Bhaskar Das,[1] Stuart Calder,[2] Ezra Day-Roberts,[1] Moumita Maiti,[1] Yeon Lee,[1] Caitlyn Komar,[1] Turan Birol,[1] and Chris Leighton[1,*]

[1]*Department of Chemical Engineering and Materials Science, University of Minnesota, Minneapolis, Minnesota 55455, USA*
[2]*Neutron Scattering Division, Oak Ridge National Laboratory, Oak Ridge, Tennessee 37830, USA*

(Received 29 July 2024; revised 1 November 2024; accepted 6 November 2024; published 25 November 2024)

Pyrite-structure NiS_2 is, in principle, a model antiferromagnetic Mott insulator that can be electron doped, hole doped, and bandwidth controlled. Despite decades of study, however, the electronic and magnetic behavior of NiS_2 have proven challenging to understand. Here, we build on recent advances establishing surface conduction in NiS_2 to completely reexamine the electronic phase behavior of electron- and hole-doped single-crystal $Ni_{1-x}Cu_xS_2$ and $Ni_{1-x}Co_xS_2$. Magnetometry, heat capacity, neutron diffraction, and electronic transport measurements suggest that prior studies missed vital details of the magnetic ordering in this system. While electron and hole doping rapidly increase the antiferromagnetic ordering temperature (by as much as fourfold by $x \approx 0.1$), signatures remain of antiferromagnetic and weak ferromagnetic ordering at the same temperatures as in undoped NiS_2. As these undoped ordering temperatures remain constant, the associated magnetic moments are diminished by doping, strongly implicating electronic/magnetic phase coexistence across the Mott insulator-metal transition. Substantial structural changes and inhomogeneity accompany these evolutions, highlighting the importance of structural-chemical-electronic-magnetic coupling in NiS_2. The insulator-metal transition is also strongly electron/hole asymmetric, which we interpret with the aid of complementary dynamical mean-field theory results. These findings significantly revise and advance our understanding of the electronic phase behavior of this prototypical Mott insulator, highlighting the essential role of electronic, magnetic, structural, and chemical inhomogeneity across the Mott transition.

DOI: 10.1103/PhysRevMaterials.8.114420

I. INTRODUCTION

The three-dimensional pyrite-structure transition-metal disulfides (TMS_2) are a notable class of materials in terms of band filling control of electronic and magnetic properties and associated functionality [1–4]. FeS_2, CoS_2, NiS_2, and CuS_2 share the same simple, cubic, pyrite structure, where TM^{2+} ions are octahedrally coordinated by $(S_2)^{2-}$ dimers, leading to $t_{2g}^6e_g^0$, $t_{2g}^6e_g^1$, $t_{2g}^6e_g^2$, and $t_{2g}^6e_g^3$ electronic configurations, respectively [1–4]. FeS_2 is thus a diamagnetic semiconductor, CoS_2 a ferromagnetic (F) metal, NiS_2 an antiferromagnetic (AF) Mott insulator, and CuS_2 a low-temperature superconductor [1–4]. Solid solutions (e.g., $Fe_{1-x}Co_xS_2$ [1,3–9]) are also stable over wide ranges between these compounds [1–18], enabling facile chemical tuning of the e_g band filling, from e_g^0 in FeS_2 to e_g^3 in CuS_2. For decades, these materials have thus been employed as model filling-tuned systems [1–18].

The above attributes are particularly useful in the study of the model AF Mott insulator NiS_2, which can be electron doped in $Ni_{1-x}Cu_xS_2$ [3,4,10,14–17], hole doped in $Ni_{1-x}Co_xS_2$ [1–4,10,12,13], and bandwidth controlled in $NiS_{2-x}Se_x$ [4,19–26]. Due in large part to this flexibility, chemically substituted NiS_2 has been heavily investigated for years, particularly in the study of the transition from Mott insulating to correlated or uncorrelated metallic states [10–26]. A partial electronic phase diagram of NiS_2 has thus been compiled vs both doping and bandwidth, generating key insights into this central problem in correlated electron physics [3,4,22,24]. It should be acknowledged, however, that there are significant gaps in the understanding of even this heavily studied system. In hole-doped $Ni_{1-x}Co_xS_2$, for example, there remain substantial regions of phase space at intermediate x in which little, if any, exploration has been performed [3,4,10,12,13]. In terms of electron doping, CuS_2 lies on the verge of stability and can only be synthesized at high pressures [27], meaning that under typical growth conditions $Ni_{1-x}Cu_xS_2$ crystals have an effective solubility limit, restricting the accessible range of electron doping [14,15]. Arguably, the most important limits to understanding, however, arise in relatively lightly electron- and hole-doped $Ni_{1-x}Cu_xS_2$ and $Ni_{1-x}Co_xS_2$ in the vicinity of the transition from Mott insulator to metal.

Two issues are particularly noteworthy with respect to the insulator-metal transition in doped NiS_2. First, the majority of studies on this system were performed prior to the realization that surface conduction dramatically impacts electronic transport in NiS_2 [28–33]. It is now understood, as it is in FeS_2 [34–43] and CoS_2 [44], that surface states are rife in single-crystal NiS_2, generating surface conductivities much higher than bulk [28–30,32]. In typical transport measurements, the

*Contact author: leighton@umn.edu

freeze-out of the Mott-insulating interior on cooling then leads to the surface shunting current at low temperature (typically below ∼100 K), resulting in surface-dominated transport [28]. This is now established from temperature (T)-dependent resistivity (ρ) measurements [28,30,32,33], thickness [28] and shape [30,33] scaling, Hall effect data [29,30], the rich surface magnetotransport effects that arise in NiS_2 crystals [28,29] and nanoflakes [32], and photoemission studies [31]. Transport data in the literature on NiS_2 doped with Co or Cu [12–16] or substituted with Se [19–23,26] show clear indications of surface conduction, but were historically interpreted as reflecting the NiS_2 *bulk*, meaning that the location and nature of the insulator-metal transitions with doping and bandwidth control have likely been mischaracterized.

Second, there are features of the electronic and magnetic behavior of NiS_2 vs doping that are extraordinary but have not been fully understood. NiS_2 exhibits a complex sequence of magnetic behaviors and transitions on cooling [1–4,10,45–55]. The face-centered-cubic array of Ni^{2+} ions creates geometrical frustration, which hinders AF ordering despite strong AF exchange interactions [23,46,48,50,53,56]. The frustration ratio θ_{CW}/T_N (where θ_{CW} is the Curie-Weiss temperature and T_N is the Néel temperature) has been reported to be as high as ∼30 [28,48], and short-range AF order has been detected above T_N [28,53,56]. Long-range AF order then kicks in at $T_N \approx 38$ K, through a typical second-order phase transformation [23,28,29,46–48,50–53,55,56], generating a spin structure that is complex and noncollinear [23,46,48,50,53,56]. Remarkably, at $T_{wf} \approx 30$ K, a second magnetic transition takes place, to a weak ferromagnetic (WF) state [15,23,28,29,46–48,51,53–56]. It is clear that this WF behavior is robust and widely observed, and that it arises through a weakly first-order transition, but the origin of the WF state is controversial, particularly given that an F moment is symmetry forbidden in the pyrite structure [23]. Structural distortions [23,50,56,57] and domain effects [51] have been proposed to explain the WF state, but the origin remains unsettled. This richness in magnetic response continues as NiS_2 is doped. The accepted magnetic phase diagram in fact shows T_N dramatically increasing with doping with both electrons and holes, reaching as high as ∼130 K (over three times the undoped T_N) by $x \approx 0.1$ [3,4,10], although this extraordinary behavior has not been fully explained [3]. T_N is then thought to gradually decrease with further doping [3,4,10], along with T_{wf} [3,4,10], although the solubility limit in $Ni_{1-x}Cu_xS_2$ and the unexplored region in the $Ni_{1-x}Co_xS_2$ phase diagram mean that this has not been fully tracked vs either electron or hole doping.

In light of the above, the motivation for the current paper is straightforward. Given the simple structure and stoichiometry of NiS_2, the ease with which it can be electron doped, hole doped, and bandwidth controlled, and that it is touted as a model AF Mott insulator, the level of uncertainty regarding key features of the NiS_2 electronic phase behavior at low doping is unacceptable. We significantly improve on this here through a detailed study of the magnetic, thermodynamic, and electronic transport properties of electron- and hole-doped NiS_2 single crystals. $Ni_{1-x}Cu_xS_2$ is studied up to an effective solubility limit of $x = 0.08$, while $Ni_{1-x}Co_xS_2$ is studied up to $x = 0.30$. Detailed investigations at ∼20 doping levels provide strong evidence that vital details of magnetic ordering in this system may have been missed in prior studies. Electron and hole doping are found to indeed rapidly stabilize T_N (by as much as fourfold by $x \approx 0.1$), but, at the same time, clear signatures persist of the T_N and T_{wf} of undoped NiS_2. As the undoped T_N and T_{wf} persist, their associated magnetic moments are diminished by doping, strongly implicating electronic/magnetic phase coexistence across an inhomogeneous Mott insulator-metal transition. Clear evidence for structural/chemical changes and inhomogeneity are also found in this regime. Doping-dependent transport measurements accounting for the intrinsic surface conduction then establish that the Mott insulator-metal transition is distinctly electron/hole asymmetric, which we interpret with the aid of complementary dynamical mean-field theory (DMFT) results. These findings establish a revised electronic phase diagram for electron- and hole-doped NiS_2, significantly altering and advancing our understanding of the electronic phase behavior of this prototypical Mott insulator.

II. METHODS

$Ni_{1-x}Cu_xS_2$ and $Ni_{1-x}Co_xS_2$ single crystals were grown by chemical vapor transport (CVT) [12–14,28,29,32,58]. Precursor powders of NiS_2, CoS_2, and CuS were first prepared. High-purity powders of Ni (Alfa Aesar, 99.999% purity), Cu (Strem Chemicals, 99.999%), Co (Alfa Aesar, 99.998%), and S (Thermo Scientific, 99.999%), in a nominal molar ratio of 1:7 (for Ni:S and Co:S) or 1:1 (for Cu:S), were thoroughly mixed and sealed in evacuated (∼10^{-6} Torr) quartz ampoules. The resulting powders were then heated to 670° C for 6 d for NiS_2, 625° C for 6 d for CoS_2, and 500° C for 1 d for CuS, followed by furnace cooling. To separate excess S during NiS_2 and CoS_2 reactions, the quartz ampoules were laid approximately horizontally in a two-zone tube furnace, with a slight downward tilt; reheating to 180–250° C separated the liquid S. Next, phase-pure NiS_2, CuS, and CoS_2 precursor powders in stoichiometric ratios corresponding to $Ni_{1-x}Cu_xS_2$ and $Ni_{1-x}Co_xS_2$ (total mass ∼2.2 g at each x), were loaded into evacuated (∼10^{-6} Torr) quartz ampoules with ∼100 mg of $NiBr_2$ (Sigma-Aldrich, 99.999%) transport agent. Crystal growth then proceeded in a two-zone tube furnace in a temperature gradient from 715° C (source) to 635° C (sink), usually for 16 d; as is typical [28,29,32,35,37,38,40,41,58,59], the hot and cold zones were inverted for 3 d at the beginning of the growth. Single crystals with average size several mm were obtained, and were cleaned in solvent to remove any residual S or $NiBr_2$. Powder x-ray diffraction (XRD) was performed on ground versions of these crystals using a Rigaku MiniFlex 600 with a Cu $K\alpha$ x-ray source and a graphite diffracted beam monochromator. Lattice parameters were subsequently obtained from whole pattern fits in JADE [60]. Energy-dispersive x-ray spectroscopy (EDS) measurements were carried out in a JEOL JSM-6010PLUS/LA scanning electron microscope with an integrated EDS detector. Spectra were collected on flat, large (few-hundred-μm) crystal surfaces, at 10 or 20 kV.

Magnetometry was performed in a Quantum Design Physical Property Measurement System (PPMS) vibrating sample

magnetometer and a Quantum Design Superconducting Quantum Interference Device magnetometer from 2 to 300 K, in applied magnetic fields (H) up to 90 kOe along [111], perpendicular to the crystal surfaces. Zero-field specific heat capacity measurements were carried out by relaxation calorimetry in a PPMS between 2 and 300 K. For standard relaxation calorimetry measurements, 2% temperature pulses were applied, and three measurements were averaged at each temperature. The thermal coupling factor was maintained above ∼95% and the ratio of sample to addenda specific heat was kept above 0.5 [61]. In order to probe phase transitions accurately, long-pulse measurements were additionally performed, using 5% or 10% temperature pulses to scan continuously through phase transitions. Transport measurements were also conducted in a PPMS, from 2 to 400 K, in a van der Pauw configuration with DC excitation. Soldered In contacts were applied to pristine, as-grown surfaces. The back (non-contacted) side of the crystals was polished to reduce the thickness to a few mm using SiC paper, followed by 3- and 1-μm diamond slurries. Neutron powder diffraction (NPD) was done on the HB-2A powder diffractometer at the High Flux Isotope Reactor (HFIR), Oak Ridge National Laboratory (ORNL). 2–3 g powder samples (ground crystals) of NiS_2, $Ni_{0.95}Co_{0.05}S_2$, and $Ni_{0.80}Co_{0.20}S_2$, contained in V cans, were measured at several temperatures from 4.2 to 200 K, counting for 4 h per scan. A finer temperature spacing was employed for order parameter measurements, counting for either 300 or 600 s per point. A constant wavelength of 2.41 Å was selected using a Ge(113) monochromator. Diffraction patterns were collected by scanning a 120° bank of 44 ^{3}He detectors in 0.05° steps, providing 2θ coverage from 5° to ∼126°. The collimation was open-open-12', and a pyrolytic graphite filter was placed before the sample to eliminate higher order reflections. Subsequent Rietveld refinement was carried out using GSAS-II [62].

DFT+DMFT calculations were performed with the Rutgers eDMFT code [63,64]. The DFT (density functional theory) portion of the calculations was performed within the local density approximation using the linearized augmented plane wave method in Wien2K [65]. A $10 \times 10 \times 10\,k-$point grid was chosen for the 12-atom primitive cell. The DMFT impurity problem was solved using the continuous time quantum Monte Carlo method included in eDMFT. As all Ni sites occupy the same Wyckoff position, only one impurity problem was treated, with all quantities on the different Ni atoms related via the symmetry operations connecting the sites. All five Ni d orbitals, including the fully occupied t_{2g} states, were treated as correlated, and states within ±10 eV of the Fermi level were included in hybridization. The "exact" double counting correction was used to determine the occupancy of the correlated orbitals [66]. The self-energy was directly sampled, with its high-frequency tail being smoothed for stability, as in Ref. [67]. The values of Hubbard U and Hund's J were set to 10.7 and 0.7 eV, respectively, consistent with other studies on $3d$ transition metals using this code [68,69]; these values are higher than they would be in DFT alone, as DMFT explicitly models electron screening. Real axis quantities were obtained via analytic continuation from the imaginary axis with a 25 meV broadening. All calculations were done at 232 K.

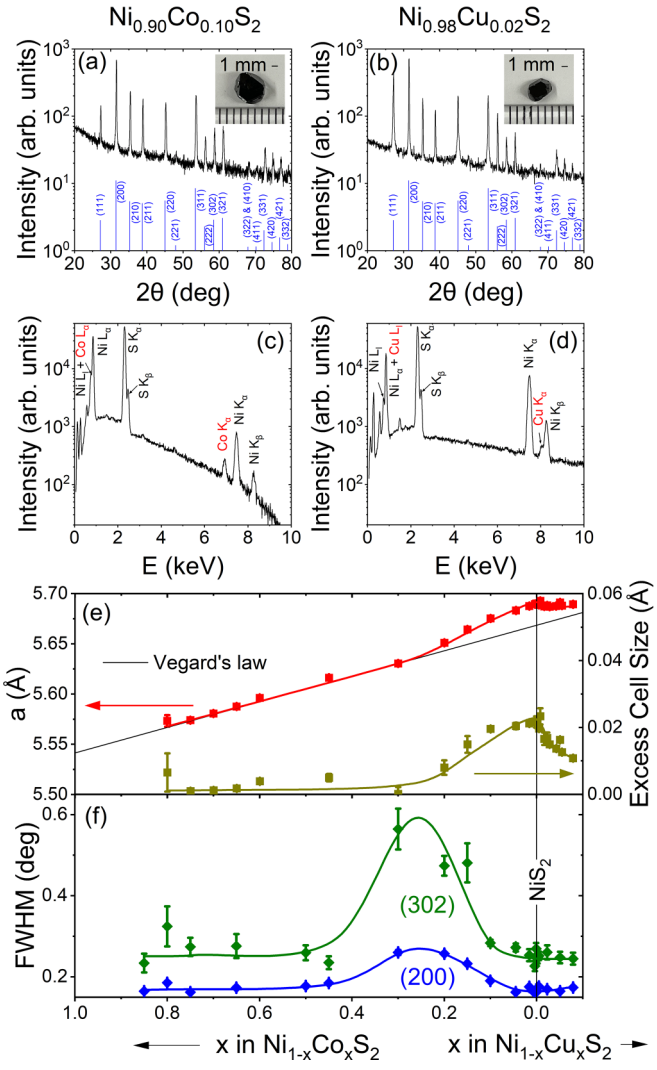

FIG. 1. Wide-angle powder x-ray diffraction (XRD) patterns (black) from representative ground crystals of (a) $Ni_{0.90}Co_{0.10}S_2$ and (b) $Ni_{0.98}Cu_{0.02}S_2$, with reference patterns (blue) [70] shown below. The insets to (a) and (b) are photographs of example corresponding crystals with a 1-mm scale bar shown. Energy-dispersive x-ray spectra from approximately $200 \times 200\,\mu m^2$ regions of representative crystals of (c) $Ni_{0.90}Co_{0.10}S_2$ and (d) $Ni_{0.98}Cu_{0.02}S_2$. Primary peaks are labeled and dopant Co and Cu peaks are labeled in red. (e) Doping (x) dependence of the cubic lattice parameter (a, left axis, red), and the excess cell size relative to the Vegard's law (solid-black line) extrapolation from the $Fe_{1-x}Co_xS_2$ system (Δa, right axis, dark yellow), for $Ni_{1-x}Co_xS_2$ (hole doping) and $Ni_{1-x}Cu_xS_2$ (electron doping). (f) Doping dependence of the XRD peak full-width at half-maximum (FWHM) for $Ni_{1-x}Co_xS_2$ (hole doping) and $Ni_{1-x}Cu_xS_2$ (electron doping). FWHM data are shown for the (200) (blue) and (302) (green) Bragg peaks. Data points and error bars in (e) were extracted from whole-pattern XRD fits; data points and error bars in (f) are from Gaussian fits to individual Bragg peaks. Colored solid lines in (e) and (f) are guides to the eye.

III. RESULTS

A. Structural and chemical characterization

The insets to Figs. 1(a) and 1(b) show photographs of representative several-mm single crystals at example

compositions of $Ni_{0.90}Co_{0.10}S_2$ (hole-doped) and $Ni_{0.98}Cu_{0.02}S_2$ (electron-doped). Corresponding XRD patterns of ground crystals at these compositions are shown in the main panels of Figs. 1(a) and 1(b) (black lines), revealing good agreement with accepted patterns for pyrite NiS_2 (blue lines) [70]. As in our prior papers on undoped NiS_2 [28,29,32,58], the crystals are thus phase-pure within the detection limits of powder XRD. Figures 1(c) and 1(d) then show corresponding EDS data, from which an average (over 24 crystals of various dopings) sulfur-to-metal ratio of 1.98 was extracted (with a standard deviation of 0.09), i.e., close to stoichiometric. For comparison, the random uncertainty on this ratio is ∼0.01, which is outweighed by the systematic uncertainty of ∼0.05. More important in the current context, Figs. 1(c) and 1(d) also show characteristic K and L peaks for Co and Cu, respectively (red labels), confirming dopant incorporation. As discussed in detail in Fig. S1 and its caption within the Supplemental Material (SM) [71], at sufficiently high x, direct determination of the actual doping was thus possible by EDS. At very low x, however, this was not possible, and so carefully calibrated EDS doping vs nominal doping relations for both $Ni_{1-x}Co_xS_2$ and $Ni_{1-x}Cu_xS_2$ (Fig. S1 within the SM [71]) were used for determination of actual x values by extrapolation. In the Cu doping case, actual doping of $x = 0.08$ could not be exceeded under our growth conditions, primarily because of preferential crystallization of CuS.

As shown in Fig. 1(e), quantitative analysis of powder XRD data provides additional insight into the structure of these doped NiS_2 crystals. The left axis shows the cubic lattice parameter (a) over a wide doping range, compared to the Vegard's law prediction based on the lattice parameter in the well-studied $Fe_{1-x}Co_xS_2$ series [3,6–8], which approximately connects with the lattice parameter of CuS_2 [3]. As previously noted [3], there is a clear expansion of the unit cell around the NiS_2 composition. This is shown more clearly on the right axis, which plots the excess lattice parameter over the Vegard's law prediction Δa, which evolves asymmetrically about the NiS_2 composition. Hole doping to $x \approx 0.3$ is needed to fully suppress Δa, while electron doping initially rapidly suppresses Δa, followed by a slower drop out to the effective solubility limit. This excess cell volume and its asymmetric doping dependence will be returned to below (Sec. III E), where they are found to be strongly correlated with the evolution of electronic and magnetic properties. Intriguingly, Fig. 1(f) reveals that as the unit-cell expansion decreases with hole (Co) doping, a broad maximum in the full-width at half-maximum (FWHM) of some of the XRD peaks arises around $x \approx 0.25$, shown here for the (200) and (302) peaks. As the powder particle size does not vary systematically with x (nor does the instrumental broadening, which is only ∼0.13° in the relevant 2θ window), this peak broadening must derive from microstrain effects, i.e., spatial distributions of local lattice spacings. This was investigated more thoroughly by refining the powder XRD patterns at each composition using GSAS-II [62] and then applying the generalized strain model within GSAS-II. As shown in Fig. S2 within the SM [71], this reveals ∼0.6% average microstrain values at $x \approx 0.25$ but with very different values of the two microstrain tensor components in cubic symmetry, the S_{220} component being large while the S_{400} component is negligible. This is a strong hint to potential local symmetry breaking in a broad doping region centered around $x \approx 0.25$, which we plan to explore in the future with additional diffuse x-ray scattering measurements and analyses. It is argued below (Sec. III E), where the data of Fig. 1(f) are correlated with electronic and magnetic properties, that these structural findings also likely point to doping inhomogeneity in certain broad x ranges.

B. Revised phase diagram

Section III C below (discussing Figs. 3–6) describes full details of the doping-dependent evolution of magnetic, thermodynamic, and transport properties of these $Ni_{1-x}Co_xS_2$ and $Ni_{1-x}Cu_xS_2$ crystals. Prior to that discussion, however, we present the revised phase diagram that results from this paper [Fig. 2(a)]. As noted in the Introduction, undoped NiS_2 exhibits two successive magnetic ordering temperatures, T_N and T_{wf}, at ∼38 K [23,28,29,46–48,50–53,55,56] and ∼30 K [15,23,28,29,46–48,51,53–56]. Consistent with prior reports, as electron or hole doping proceeds, doped samples then exhibit a doped Néel temperature T_{ND} [green points in Fig. 2(a)] that increases rapidly with x [3,4,10,22]. For hole doping with Co, the increase in T_{ND} is smooth, reaching ∼150 K by $x = 0.10$, beyond which a weak decrease occurs. While the increase in T_{ND} for electron doping with Cu is also rapid (reaching ∼130 K by $x = 0.08$), electron/hole doping asymmetry is clear. Specifically, T_{ND} increases quickly with initial electron doping, reaches a narrow plateau around $x = 0.01$, then increases again before slowing near the effective Cu solubility limit. The prior claims of rapidly increasing T_{ND} with increasing electron and hole doping [3,4,10,22] are thus substantiated, but with significant quantitative differences, particularly the electron/hole doping asymmetry.

What was apparently missed in prior studies, however, is that as T_{ND} increases with x, there remain subtle but clear indications of T_N and T_{wf} at temperatures that barely deviate from their undoped values [red and blue points in Fig. 2(a)]. This magnetism apparently associated with undoped NiS_2 is suppressed with doping not through a decrease of the ordering temperatures, but instead a decrease of the associated ordered moments. This is illustrated in Fig. 2(b), where the WF magnetization (M_{wf}) becomes undetectable by Co doping of $x = 0.10$ and Cu doping of $x = 0.03$ [which is why the T_{wf} points in Fig. 2(a) cease to be plotted], again asymmetrically with respect to electron/hole doping. Also shown in Figs. 2(a) and 2(b) are the positions of the transitions from insulator (I) to metal (M), marked by the vertical dashed lines. Importantly, and as detailed in Sec. III C, these are determined from bulk transport properties, above the temperature-dependent crossover to surface-dominated conduction [28–33]. The correlation with magnetic ordering is evident: The insulator-metal boundaries align exactly with the saturation of the doped Néel temperatures T_{ND} [Fig. 2(a)], also reflecting the same electron/hole asymmetry visible in $T_{ND}(x)$ [Fig. 2(a)] and $M_{wf}(x)$ [Fig. 2(b)].

As emphasized below (in Secs. III C, III D, and III E), the phase behavior in Figs. 2(a) and 2(b) is suggestive of an inhomogeneous Mott insulator to metal transition, progressing through a regime of electronic and magnetic inhomogeneity. We contend throughout this paper that this picture in fact

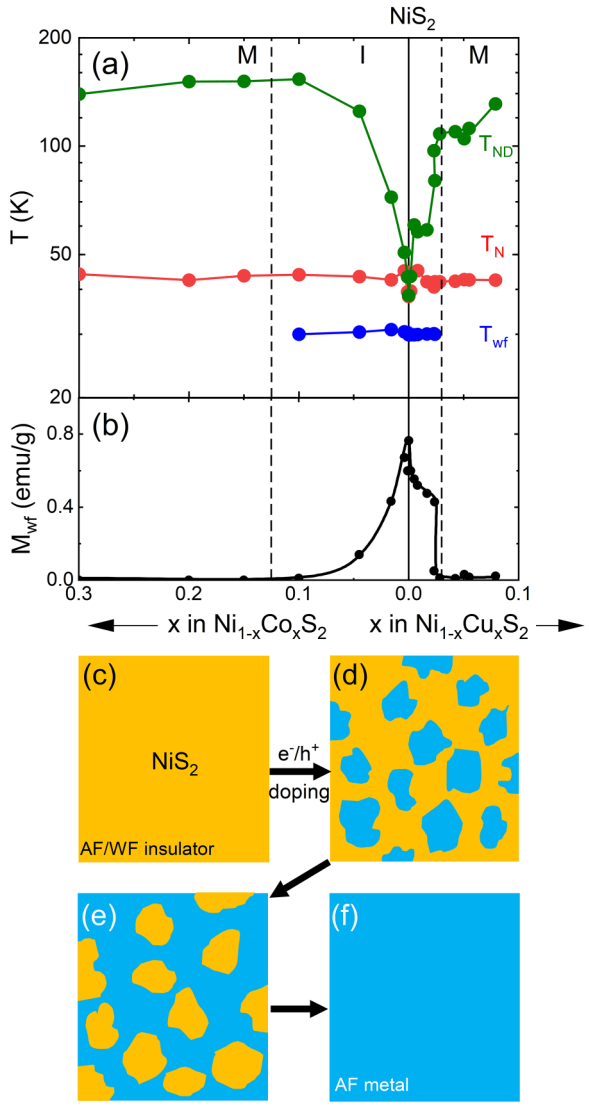

FIG. 2. (a) Revised magnetic phase diagram of hole- and electron-doped NiS_2. The region of focus involves electron-doped $Ni_{1-x}Cu_xS_2$ up to $x = 0.08$ and hole-doped $Ni_{1-x}Co_xS_2$ up to $x = 0.30$. Shown are the weak ferromagnetic (WF) transition temperature T_{wf} (blue), antiferromagnetic (AF) transition temperature T_N (red) of the near-undoped regions, and AF transition temperature T_{ND} (green) of the heavily doped regions, as determined from magnetometry and heat capacity data. Vertical dashed lines mark the Mott insulator (I)-metal (M) transition boundaries, as determined from *bulk* electronic transport data. (b) Doping (x) dependence of the WF magnetization M_{wf} of hole-doped $Ni_{1-x}Co_xS_2$ and electron-doped $Ni_{1-x}Cu_xS_2$ single crystals, as determined from zero-field extrapolations of linear fits to high-field magnetization vs field data [Figs. 3(k)−3(o)]. (c)−(f) Schematics of the proposed phase evolution with electron or hole doping (x). As x is increased, the AF/WF Mott-insulating phase in NiS_2 (yellow) transforms into an AF metallic phase (blue), through a regime of electronic/magnetic phase coexistence.

provides the only simple interpretation of the data, particularly the broad coexistence of a strongly doping-dependent T_{ND} with a T_N that is essentially unshifted from pure NiS_2, the suppression of the undoped AF/WF order occurring through gradual decrease of the ordered moment [Fig. 2(b)] rather than the ordering temperatures [Fig. 2(a)]. A schematic illustration is shown in Figs. 2(c)–2(f), in which an initially uniform AF/WF Mott-insulating phase [Fig. 2(c)] is broken up by electron/hole doping via nucleation of higher-T_{ND} AF metallic regions in a matrix of essentially undoped AF/WF insulating regions. As shown in Fig. 2(a), the doped regions have T_{ND} that increases rapidly with x. Eventually, the phase fractions invert [Fig. 2(e)], before a uniform high-T_{ND} AF metallic phase emerges [Fig. 2(f)]. From Figs. 2(a) and 2(b) it is clear that the process in Figs. 2(c)–2(f) is somewhat asymmetric with respect to electron/hole doping, while from Figs. 1(e) and 1(f) (and Fig. S2 within the SM [71]) it is clear that there are correlations with the structure and chemistry. This evidences coupling between the structure/chemistry, and electronic/magnetic properties of doped NiS_2 across the Mott transition. Section III C next provides a detailed description of the magnetic, thermodynamic, and transport data that were used to generate the phase diagram of Fig. 2(a).

C. Magnetometry, heat capacity, neutron diffraction, and electronic transport

Shown first in Figs. 3(a)–3(e) are T-dependent magnetization (M) data in an applied magnetic field (H) of 1000 Oe, under both field-cooled (FC) and zero-field-cooled (ZFC) conditions, at five representative dopings. Starting with undoped NiS_2 [Fig. 3(c)], the onset of WF order at T_{wf} is readily apparent at ∼30 K, where the FC $M(T)$ rises in an order-parameter-like fashion while the FC and ZFC curves bifurcate [3,4,23,28,46–48,51,56]. The AF ordering at T_N is clearer in Fig. 3(h), which is a close-up of the ZFC $M(T)$ from Fig. 3(c). A T_N of 39.7 K is inferred from the peak (as confirmed by neutron diffraction below). This is in reasonable agreement with prior work [23,28,29,46–48,50–53,55,56], within the range of the variations in T_N that can occur due to Ni/S stoichiometry variations. These variations are shown explicitly in Fig. S3 within the SM [71], which shows the effect of the S:Ni loading in the crystal growth tube on the structural, magnetic, and transport properties of NiS_2.

Doping, whether with holes (Co) or electrons (Cu), suppresses M_{wf}, as shown in Figs. 3(a), 3(b), 3(d), and 3(e), respectively (note the widely varying M-axis scales). Hole doping to $x = 0.05$ [Fig. 3(b)] suppresses M_{wf} by a factor of ∼70, but, as highlighted in Sec. III B, T_{wf} remains unchanged at ∼30 K. A new feature emerges at higher T (∼100 K), however, where a second FC/ZFC bifurcation arises, albeit weak. Increasing the hole doping to $x = 0.20$ [Fig. 3(a)] then essentially eradicates any sign of the original WF order (note the M-axis scale) but leads to clearer FC/ZFC splitting at even higher T (∼150 K). It is shown below from neutron diffraction that the temperature at which this FC/ZFC splitting turns on is definitively a Néel transition, and thus we label it T_{ND}, the doped Néel temperature. Importantly, as this strong evolution of M_{wf} and T_{ND} with hole doping takes place, the close-ups in Figs. 3(f) and 3(g) reveal that a clear signature of the undoped T_N remains. Qualitatively similar behavior takes place with electron doping with Cu but with differences in doping scales. As shown in Figs. 3(d) and 3(i), M_{wf} is suppressed by a factor of ∼10 by only $x = 0.02$ [Fig. 3(d)], while T_{wf} is unaffected [Fig. 3(d)], and the undoped T_N remains visible [Fig. 3(i)].

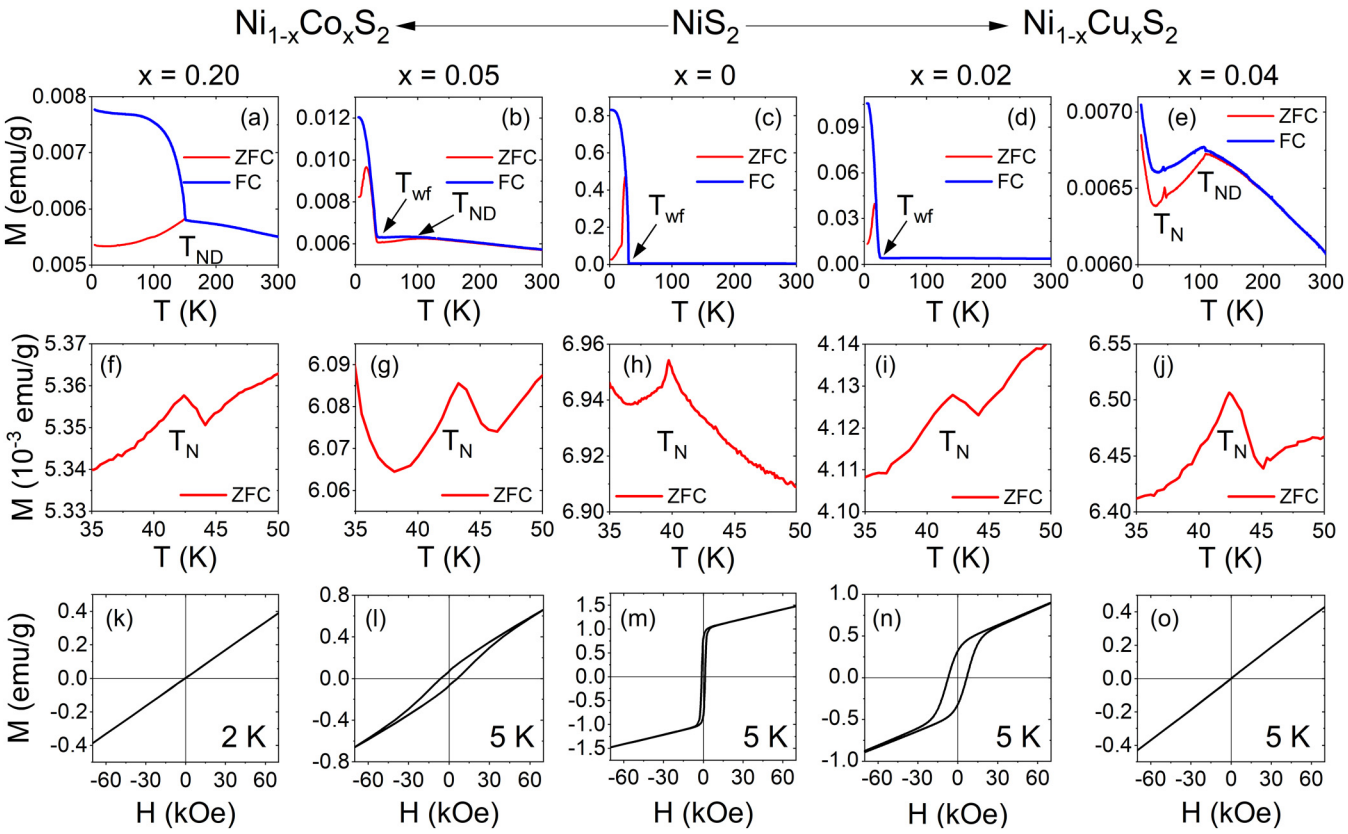

FIG. 3. (a)–(e) Temperature (T) dependence of the FC (field-cooled, blue) and ZFC (zero-field-cooled, red) magnetization (M) of five representative hole- or electron-doped $Ni_{1-x}Co_xS_2$ and $Ni_{1-x}Cu_xS_2$ crystals, in a 1000-Oe applied field (H). When present, T_{wf}, T_N, and T_{ND} are labeled in each panel. (f)–(j) Close-up of the ZFC $M(T)$ curves in (a)–(e) in the vicinity of T_N. (k)–(o) M vs H curves at low-T (2–5 K) for the crystals shown in (a)–(j).

By $x = 0.04$, WF ordering is no longer apparent, and a clear T_{ND} has emerged at ∼110 K [Fig. 3(e)], but the undoped T_N again remains [Fig. 3(j)]. Figures 3(b)–3(d) and 3(f)–3(j) in fact show only minimal variations in T_{wf} (< 1.2 K) and T_N (< 4.5 K) with doping [see also Fig. 2(a)], which we show in Fig. S3 within the SM [71] to be comparable to the range due to minor deviations from ideal metal/sulfur ratio.

Complementary to $M(T)$, Figs. 3(k)–3(o) show $M(H)$ at low T (2–5 K). The WF behavior in undoped NiS_2 [Fig. 3(m)] manifests as clear low-field hysteresis from the WF component, superimposed on a linear "background" from the AF component [28,29,47,51,56]. Hole doping to $x = 0.05$ [Fig. 3(l)] or electron doping to $x = 0.02$ [Fig. 3(n)] suppresses the remnant magnetization, which then vanishes at higher doping [Figs. 3(k) and 3(o)], consistent with the eradication of the WF signature in $M(T)$ in Figs. 3(a) and 3(e). This is all reflected in the electron/hole-asymmetric $M_{wf}(x)$ shown in Fig. 2(b), which was extracted by extrapolating the high-field (> 60 kOe) portion of the $M(H)$ curves in Figs. 3(k)–3(o) to $H = 0$. Note that nontrivial doping variations in the coercivity are also apparent in Figs. 3(k)–3(o), as returned to and explained in Sec. III D below.

The overall picture from the magnetometry data of Fig. 3 is clear. T_{ND} indeed rapidly increases with increasing electron or hole doping, as reported previously [3,4,10], but at the same time clear signatures of T_{wf} and T_N remain, essentially invariant from undoped NiS_2 [as in Fig. 2(a)]. M_{wf} is suppressed with doping, however [with some asymmetry between electron and hole doping, Fig. 2(b)], strongly suggestive of magnetic phase separation into spatial regions with doped, and near-undoped, magnetic properties [Figs. 2(d) and 2(e)].

T-dependent specific heat capacity (C_p) measurements at the same five representative electron and hole dopings are shown in Fig. 4, providing further insight. Shown first in Fig. 4(c) is the $C_p(T)$ of undoped NiS_2 between 2.5 and 300 K, measured in both standard relaxation (short pulse, black data) and scanning (long pulse, red data) modes (see Sec. II for measurement details). $C_p(T)$ displays the expected overall increase with increasing T, approaching $3R$ (where R is the molar gas constant) above 300 K, but with a large, sharp peak at ∼30 K owing to T_{wf}. This peak is higher in long-pulse-mode data, consistent with the weakly first-order nature of the WF transition [15,23,28,29,46–48,51,53–56]. A close-up of the long pulse $C_p(T)$ data is shown in Fig. 4(h), revealing also a second, smaller peak at ∼38 K owing to T_N. This latter peak is essentially identical in short- and long-pulse measurements, consistent with its second-order nature [23,28,29,46–48,50–53,55,56]. Overall, this heat capacity behavior is in agreement with prior reports on undoped NiS_2 [10,48]. The effect of electron and hole doping is then shown in Figs. 4(a), 4(b), 4(d), 4(e) and Figs. 4(f), 4(g), 4(i), 4(j). Entirely consistent with the deductions from magnetometry (Fig. 3), three main trends are apparent. First, electron and hole doping suppress

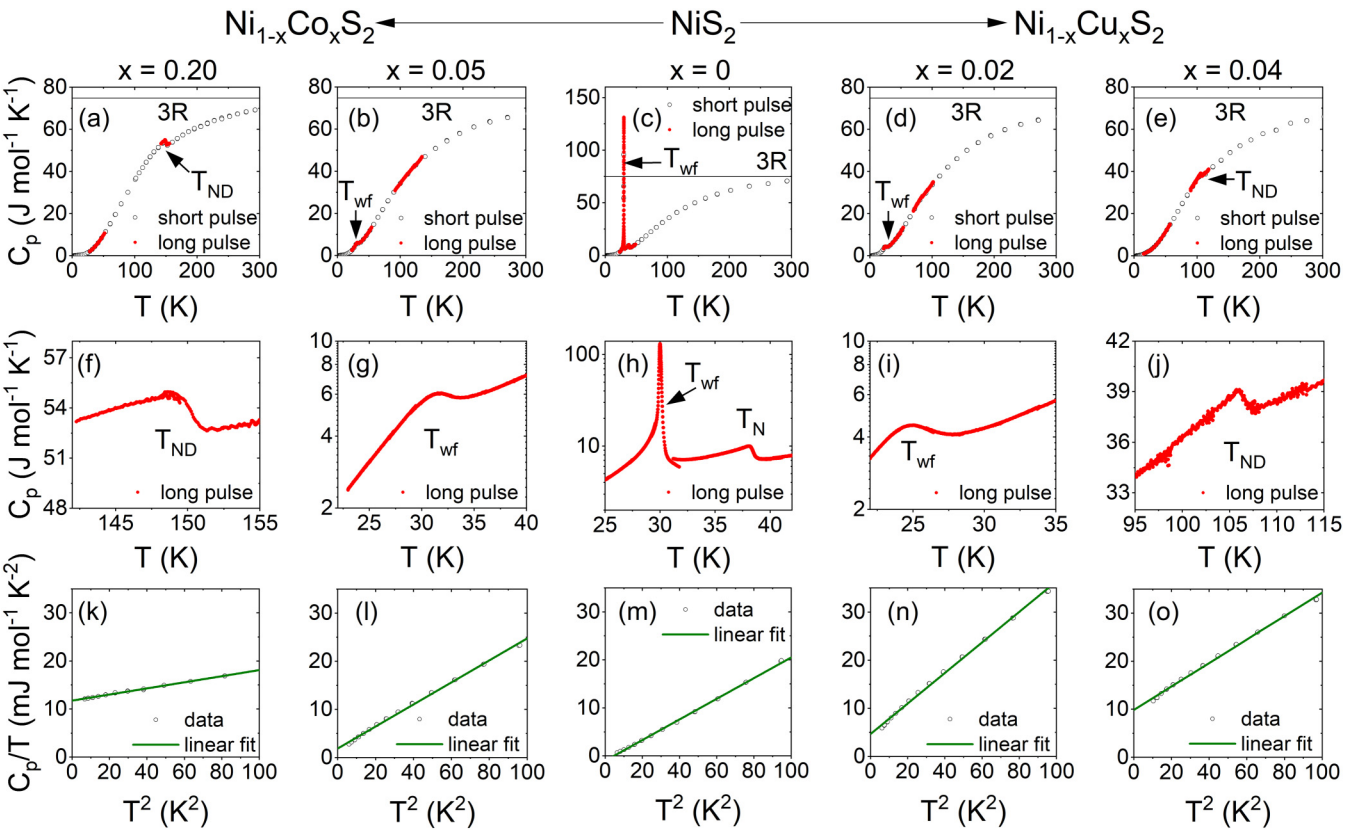

FIG. 4. (a)–(e) Temperature (T) dependence of the specific heat (C_p) of five representative hole- or electron-doped $Ni_{1-x}Co_xS_2$ and $Ni_{1-x}Cu_xS_2$ crystals. The black-open circles and the red-filled circles were obtained in relaxation (short pulse) and scanning (long pulse) modes, respectively. The Dulong-Petit $3R$ limit (R is the molar gas constant) is shown, and, when present, T_{wf}, T_N, and T_{ND} are labeled in each panel. (f)–(j) Close-up of the long-pulse $C_p(T)$ in (a)–(e) in the vicinity of T_{wf}, T_N, or T_{ND}. (k)–(o) Low-T (up to 10 K) C_p/T vs T^2 plots for the crystals shown in (a)–(j). Short-pulse data (black circles) are shown along with linear fits (green lines); note the doping evolution of the $T = 0$ intercept, which is the Sommerfeld coefficient γ.

the signature of WF order, asymmetrically with respect to electrons/holes. Hole doping to $x = 0.05$ and electron doping to $x = 0.02$ [Figs. 4(b), 4(d), 4(g), and 4(i)] decrease the C_p peak height at T_{wf} from $\sim$130 J mol^{-1}K^{-1} in undoped NiS_2 to only 5−6 J mol^{-1}K^{-1}, further doping [Figs. 4(a), 4(e), 4(f), and 4(j)] eradicating this signature all together. Second, as this happens, T_{wf} remains essentially unshifted from the undoped position, as can be seen by comparing Figs. 4(g), 4(i), and 4(h). Significant broadening of the transition is evident, however, which is unsurprising given that it likely arises from small regions with low, but likely nonzero, doping [blue in Fig. 2(d)]. Third, at the highest electron and hole dopings [Figs. 4(a), 4(e), 4(f), and 4(j)], clear signatures of T_{ND} emerge, at temperatures coincident with the FC/ZFC splittings in $M(T)$ [Figs. 3(a) and 3(e)], as reported by Ogawa *et al.* [10].

Further analyzing the low-T $C_p(T)$ behavior, Figs. 4(k)–4(o) show sub-10-K C_p/T vs T^2 plots, to test for adherence to $C_p(T) = \gamma T + \beta T^3$. Here, γT is the electronic contribution to C_p, where γ is the Sommerfeld coefficient, and the βT^3 term is the low-T expansion of the Debye-model vibrational heat capacity [72–74]. In the latter, $\beta = 234\,Nk_B/\theta_D^3$, where N is the number of atoms per mole, k_B is Boltzmann's constant, and θ_D is the Debye temperature [72–74]. This form is well adhered to in all cases, as illustrated by the green straight-line fits in Figs. 4(k)–4(o). In undoped NiS_2 [Fig. 4(m)], as expected, γ (the $T = 0$ intercept) is negligible due to the Mott-insulating ground state. Hole doping to $x = 0.05$ and electron doping to $x = 0.02$ [Figs. 4(l) and 4(n)]; however, both induce finite γ, indicating the presence of clear electronic contributions to $C_p(T)$ as $T \to 0$. This is highly significant, as [see Fig. 2(a)], these compositions remain on the insulating side of the insulator-metal transition according to bulk transport measurements. This is further strong evidence of local metallic regions in an insulating matrix, i.e., the electronic/magnetic phase coexistence illustrated in Fig. 2(d) [75,76]. With further doping, γ reaches a substantial $\sim$10 mJ mol^{-1} K^{-2} in $Ni_{0.80}Co_{0.20}S_2$ [Fig. 4(k)] and $Ni_{0.96}Cu_{0.04}S_2$ [Fig. 4(o)], in the metallic phase. It is evident from the slopes in Figs. 4(k)–4(o) that electron and hole doping also introduce asymmetric changes in θ_D. This is most evident from comparing Fig. 4(m) with Fig. 4(k), which yield θ_D for undoped NiS_2 and $Ni_{0.80}Co_{0.20}S_2$ of $\sim$300 and $\sim$450 K, respectively. While some contributions to $C_p(T)$ from magnetic excitations likely arise, complicating matters, the obvious explanation for this substantial increase in θ_D with hole doping is lattice stiffening associated with the suppression of the unit-cell volume in Fig. 1(e); we return to this below in Sec. III D.

As a final comment on Fig. 4, we note that our measurements of the doping dependence of γ are in reasonable

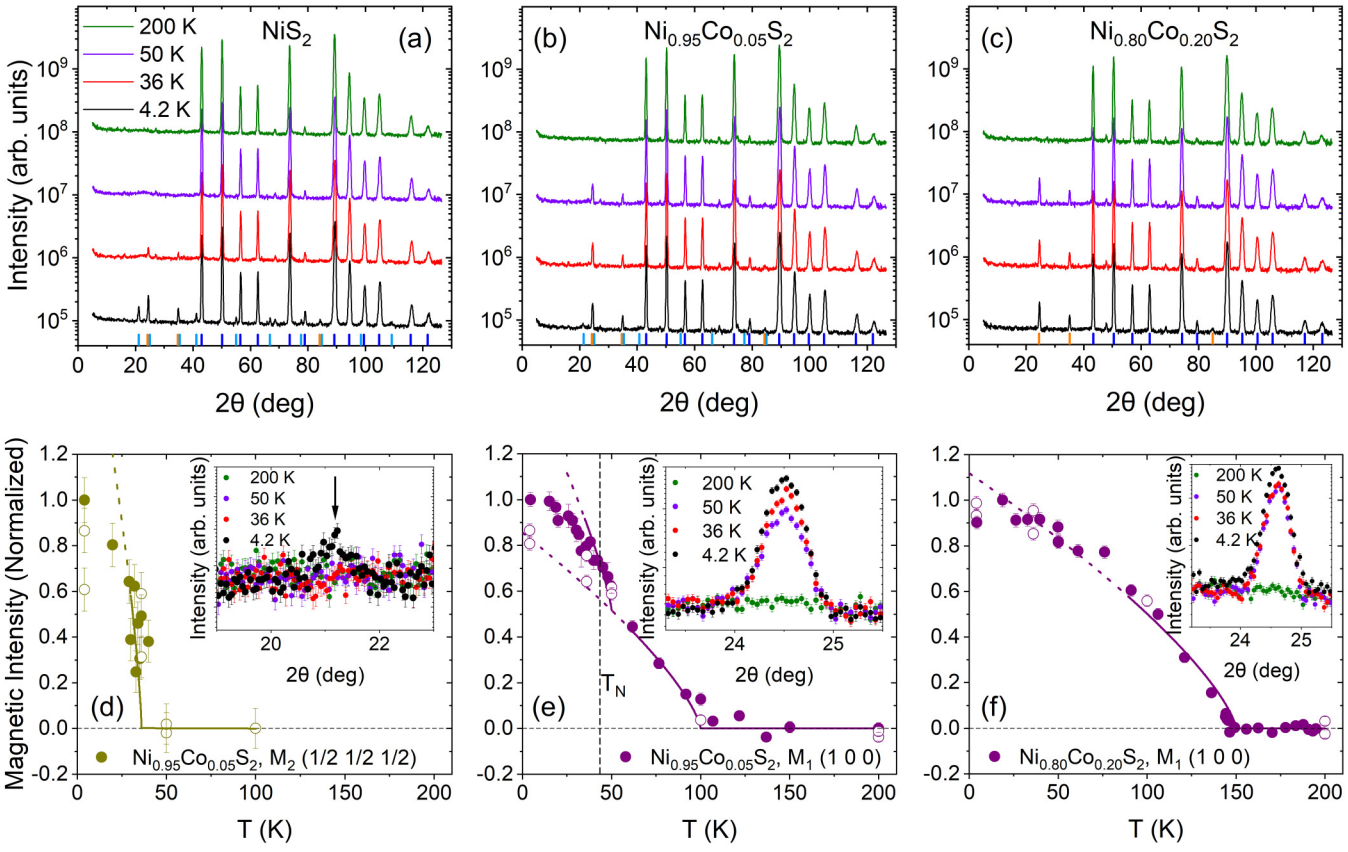

FIG. 5. Neutron powder diffraction patterns from ground crystals of (a) NiS_2, (b) $Ni_{0.95}Co_{0.05}S_2$, and (c) $Ni_{0.80}Co_{0.20}S_2$ at 4.2, 36, 50, and 200 K. The vertical-solid lines at the bottom of each panel indicate the 2θ positions of the nuclear reflections (dark blue), magnetic reflections from the M_1 phase ($T \leqslant T_N$, orange) and the M_2 phase ($T \leqslant T_{wf}$, light blue). Temperature (T) dependence of the normalized neutron diffraction intensity, for the M_1 (1 0 0) (e), (f) and M_2 (1/2 1/2 1/2) (d) reflections from $Ni_{0.95}Co_{0.05}S_2$ and $Ni_{0.80}Co_{0.20}S_2$, as labeled in the plots. The corresponding magnetic peaks are plotted in the insets to (d)–(f), which are blowups of the NPD data in (a)–(c). Solid points are from order parameter measurements with fine T spacing, while open points are from whole-pattern measurements like (a)−(c). Solid lines are critical-region fits, as discussed in the text, while dashed lines are lower-T extrapolations of these fits. In (e), the second solid line at low T is a similar fit to a second magnetic ordering at T_N, as described in the text. Error bars are standard errors on counts.

agreement a prior study, with the exception of the highest Cu dopings probed [10]. In that regime (see Fig. S1 within the SM [71]) the actual (EDS) Cu concentration differs significantly from the nominal Cu concentration, which is one potential source of such discrepancies, if sufficiently careful measurements of the actual doping level are not made (Fig. S1 within the SM [71]). Small deviations of our extracted θ_D values this prior paper [10] can be attributed to different analysis methods, specifically low-T analysis of the type shown in Figs. 4(k)–4(o) vs high-T Debye-model fits.

Direct confirmation of the doping- and T-dependent sequence of magnetic orderings in these electron/hole doped NiS_2 crystals was achieved via neutron diffraction. Measurements were made on ground crystals of undoped NiS_2, as well as hole-doped $Ni_{1-x}Co_xS_2$ with representative x values of 0.05 and 0.20. Figures 5(a)–5(c) show neutron diffraction patterns collected at 200, 50, 36, and 4.2 K for $x = 0$, 0.05, and 0.20, respectively. These temperatures were selected to capture the behavior above the maximum T_{ND}, below the maximum T_{ND}, between T_N and T_{wf}, and below T_{wf} [see Fig. 2(a)]. As noted in the Introduction, the spin structure of NiS_2 is complex. Adopting the notation used in Ref. [23] for undoped NiS_2, the magnetic structure at $T_{wf} \leqslant T < T_N$ is referred to as M_1, with a characteristic wave vector $k = (000)$, and the magnetic structure at $T < T_{wf}$ is referred to as M_2, with a characteristic wave vector $k = (1/2\,1/2\,1/2)$ [23,48,50,53]. In undoped NiS_2 [Fig. 5(a)] no magnetic order is present at 200 K and therefore all observed Bragg peaks are from nuclear reflections, as indicated by the dark blue reference lines at the bottom of panels (a)−(c). Upon further cooling, three magnetic Bragg peaks first appear at 36 K, from the AF order onsetting at T_N. The M_1 (1 0 0), M_1 (1 1 0), and M_1 (3 1 0) peaks can be seen at $2\theta = 24.5^\circ$, 34.9°, and 84.3°, respectively (see the orange reference lines at the bottom of the figure). Further cooling to 4.2 K ($< T_{wf}$) then generates additional magnetic Bragg peaks due to the M_2 magnetic structure, such as M_2 (1/2 1/2 1/2) at $2\theta = 21.1^\circ$ and M_2 (1/2 1/2 3/2) at $2\theta = 41.2^\circ$ (see the light-blue reference lines at the bottom of the figure). Note that M_2 contributes to the intensities of both M_1 (1 0 0) and M_1 (1 1 0) below T_{wf}, as these two forms of magnetic structure coexist in that T range [23,46,48].

Moving to $Ni_{0.95}Co_{0.05}S_2$ [Fig. 5(b)], comparison to the undoped case [Fig. 5(a)] reveals two clear differences. First,

the signatures of WF order (light-blue lines at the bottom of the figure) are significantly weakened, consistent with our conclusions from magnetometry (Fig. 3) and heat capacity (Fig. 4). Second, the magnetic Bragg peaks of the M_1 structure are clearly already present at 50 K, meaning that T_{ND} exceeds T_N, again consistent with above. In $Ni_{0.80}Co_{0.20}S_2$ [Fig. 5(c)], all signatures of WF order are then eradicated, leaving only M_1 peaks (orange lines at the bottom of the figure), which are now pronounced even at 50 K. To determine the onset temperatures of the M_1 and M_2 magnetic orders, the normalized intensity (I) of the M_2 (1/2 1/2 1/2) peak for $Ni_{0.95}Co_{0.05}S_2$, and M_1 (1 0 0) peak for both $Ni_{0.95}Co_{0.05}S_2$ and $Ni_{0.80}Co_{0.20}S_2$ were measured at smaller T spacing, as shown in Figs. 5(d)–5(f). For $Ni_{0.95}Co_{0.05}S_2$, the M_2 (1/2 1/2 1/2) intensity shows negligible T dependence from 200 K down to 50 K, below which it measurably rises at T_{wf} [see the inset to Fig. 5(d) for a blow-up of Fig. 5(a), where the black arrow marks the relevant magnetic reflection]. The main panel of Fig. 5(d) shows a corresponding order parameter measured with improved statistics, which is well fit near T_{wf} by $I \propto (1-T/T_{wf})^{2\beta}$, where β was fixed at 0.365, the 3D Heisenberg exponent [48,54,77] (we use a second-order phase transition approach here, as the WF ordering is known to be only weakly first order [15,23,28,29,46–48,51,53,54,56,69]. Figure 5(e) then focuses on the M_1 (1 0 0) reflection at the same doping ($x = 0.05$), showing in the inset the strong increase in this magnetic intensity between 200 and 50 K. The corresponding order parameter [main panel of Fig. 5(e)], is well fit near T_{ND} by $I \propto (1-T/T_{ND})^{2\beta}$ with $\beta = 0.365$ for the 3D Heisenberg exponent, yielding $T_{ND} \approx 100$ K. The latter is in good agreement with magnetometry [Fig. 3(b)]. What is notable in Fig. 5(e), however, is the upward deviation of the data from the fit near the undoped T_N [the dashed line is an extrapolation of the $(1-T/T_{ND})^{2\beta}$ fit]. This upward deviation is in fact well captured by a second-order parameter (second solid line) with critical temperature ~50 K. This is further strong evidence of phase coexistence of a high-T_{ND} AF metallic phase with a low-T_N AF Mott-insulating phase, as depicted in Figs. 2(d) and 2(e), the slight enhancement of the apparent T_N relative to the undoped case potentially reflecting some short-range order detectable in neutron diffraction. Finally, Fig. 5(f) shows the equivalent data for $Ni_{0.80}Co_{0.20}S_2$, where the normalized M_1 (1 0 0) intensity rises according to $I \propto (1-T/T_{ND})^{2\beta}$ with $\beta = 0.365$, yielding $T_{ND} \approx 150$ K, again in agreement with magnetometry [Fig. 3(a)] and heat capacity [Fig. 4(f)]. At this doping, unlike $x = 0.05$, no additional intensity is observed at low T, as expected due to the doping-induced suppression of the signatures of T_N and T_{wf}.

These neutron diffraction observations directly confirm our conclusions from magnetometry and heat capacity. Specifically, the T_{ND} temperature scale is indeed due to AF ordering that is rapidly stabilized by doping, the T_{wf} and T_N of undoped NiS_2 indeed persist over some doping range (where magnetic ordering at T_{ND} and T_N coexist [see Fig. 5(e)], and sufficiently heavy doping does eventually lead to a state dominated purely by AF ordering at T_{ND}. As an aside, we note that the signature of high-T_{ND} AF ordering in $M(T)$ in Figs. 3(a) and 3(e) may be somewhat atypical, but neutron diffraction data such as those in Figs. 5(c) and 5(f) unambiguously establish M_1-type AF order. To tie these conclusions regarding magnetic behavior to electronic transport properties, we now move on to doping- and T-dependent resistivity measurements.

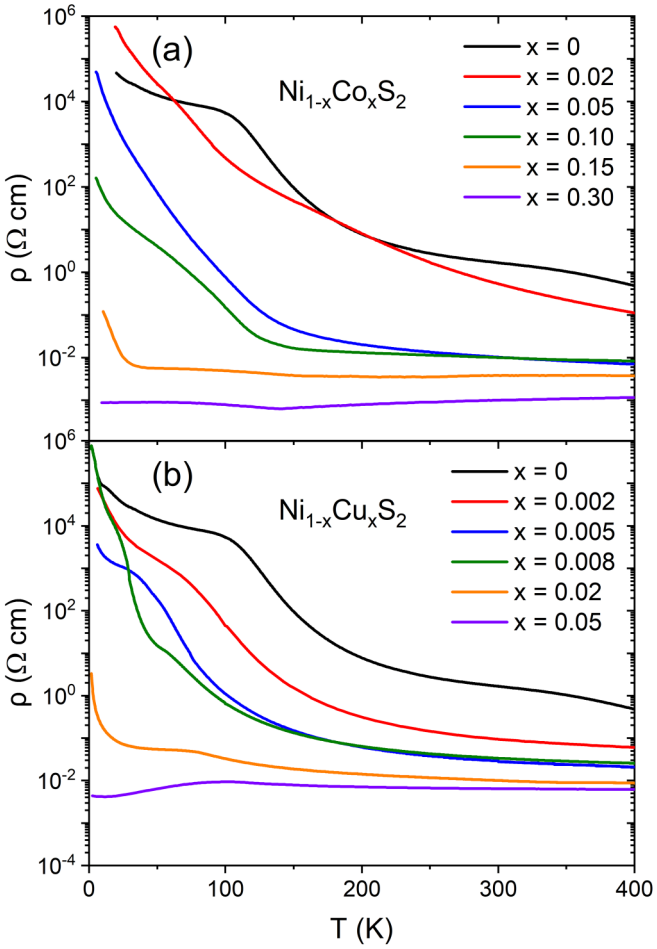

FIG. 6. Temperature (T) dependence of the electrical resistivity (ρ) of representative crystals of (a) hole-doped $Ni_{1-x}Co_xS_2$ and (b) electron-doped $Ni_{1-x}Cu_xS_2$, at various x. All measurements were performed with contacts on the pristine top surfaces of single crystals polished from the back to 1–2-mm thickness.

Figures 6(a) and 6(b) show $\rho(T)$ data for undoped NiS_2 along with a total of 10 compositions of hole-doped [Fig. 6(a)] and electron-doped [Fig. 6(b)] $Ni_{1-x}Co_xS_2$ and $Ni_{1-x}Cu_xS_2$. As noted in Sec. II, these measurements were performed by contacting pristine, as-grown crystal top surfaces. In undoped NiS_2 [black curves in both Figs. 6(a) and 6(b)], $\rho(T)$ is quantitatively consistent with our prior work [28,58], clearly reflecting surface conduction. $\rho(T)$ is insulating in nature on cooling from 400 K (with an activation energy of ~155 meV [28,48,51,52]), before abruptly flattening at ~100 K. This behavior is due to the Mott-insulating bulk (i.e., the crystal interior) freezing out on cooling, leading to the more conductive surface shunting essentially all current at $T << 100$ K [28–30]. In as-grown crystals, the low-T surface conduction is weakly metallic to weakly insulating, occurring in a few-nm-thick surface region [28]. With respect to connections to magnetic ordering, it is shown in Fig. S4 within the SM [71], consistent with prior reports [28,29,51,52], that $d\rho/dT$ reveals clear anomalies in undoped NiS_2 at both the undoped T_N

and T_{wf}. Consistent with the other conclusions in this paper, these anomalies persist with doping, up to the insulator-metal boundary (Fig. S4 within the SM [71]).

With both hole and electron doping, in $Ni_{1-x}Co_xS_2$ [Fig. 6(a)] and $Ni_{1-x}Cu_xS_2$ [Fig. 6(b)], respectively, the high-T bulk-dominated behavior evolves strongly with x. In $Ni_{1-x}Co_xS_2$, ρ(300 K) decreases monotonically and gradually with x, falling by almost three orders of magnitude by $x = 0.30$. As this occurs, $\rho(T)$ transitions from insulating-like ($d\rho/dT < 0$) to metallic-like ($d\rho/dT > 0$), the bulk insulator-metal transition apparently occurring at $x \approx 0.125$ [between the green and orange curves in Fig. 6(a)], as labeled in Fig. 2(a). We note that this position of the insulator-metal transition is necessarily, albeit not ideally, determined from relatively high-T behavior, as surface conduction prevents ready access to bulk low-T transport. Inflection points in $\rho(T)$ in fact arise at all x in Fig. 6(a), which must now surely be understood to reflect crossovers from bulk- to surface-dominated conduction. This was not appreciated in many prior studies, particularly on the Mott insulator-metal transition in $NiS_{2-x}Se_x$ [19–23,26]. As elucidated in detail in the better-understood case of FeS_2, as a function of bulk doping level, surface conduction can in fact result in various unusual forms of $\rho(T)$ [37,38,40]. This is because of the competition between doping-dependent bulk conduction, high-conductivity surface conduction, and the strongly T-dependent Schottky and/or p-n junctions that necessarily arise between the bulk and surface regions [37,38,40]. In particular, the crossover from flattening in $\rho(T)$ at low T in undoped NiS_2 in Fig. 6(a) to the sharp increases on cooling that take place at $x = 0.05$, 0.10, and 0.15, are highly reminiscent of the behavior in heavily doped FeS_2, reflecting the strongly T-dependent freeze-out of the bulk/surface junction [37,38,40]. Only deep in the metallic regime [$x = 0.30$ in Fig. 6(a)] does fairly well-behaved metallic $\rho(T)$ emerge at all T, when both the bulk and surface are metallic, and thus no significant junction arises at their interface.

Comparing to $Ni_{1-x}Cu_xS_2$ [Fig. 6(b)], the asymmetry between hole and electron doping is again apparent. ρ(300 K) falls rapidly from $x = 0$ to $x = 0.02$, reaching $\sim 1 \times 10^{-2}$ Ωcm, a resistivity that would require hole doping to $x \approx 0.10$ [Fig. 6(a)], i.e., five times heavier. Increasing x in $Ni_{1-x}Cu_xS_2$ to 0.05 then results in only weak additional decreases in ρ(300 K) before the effective solubility limit is encountered. Based on the relatively high-T (bulk-dominated) $d\rho/dT$, however, the insulator-metal transition is indeed crossed at electron doping of $x \approx 0.03$ [between the orange and purple curves in Fig. 6(b)], as marked in Fig. 2(a). At lower T, the inflection points in $\rho(T)$ that are the telltale sign of surface conduction again arise, with a roughly similar overall doping-driven evolution to the hole doping case in Fig. 6(a). As elaborated in the SM [71] (Fig. S5 and its caption), it is informative to compare the data of Fig. 6 with the data on $Ni_{1-x}Co_xS_2$ and $Ni_{1-x}Cu_xS_2$ from the Dresselhaus and Adler groups from the late 1970′s to early 1980′s [12–14]. Those data were acquired only down to just below 100 K [12–14], and thus missed the onset of surface conduction, but are nevertheless in reasonable agreement with our high-T data, albeit over a smaller doping range for $Ni_{1-x}Co_xS_2$.

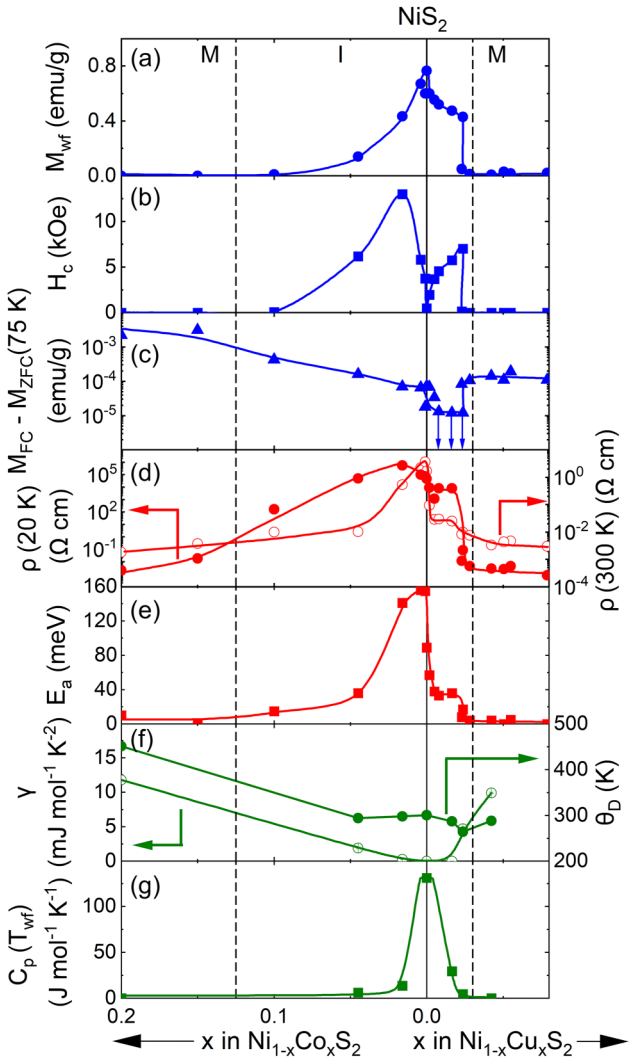

FIG. 7. Doping (x) dependence of extracted magnetic and electronic parameters for hole-doped $Ni_{1-x}Co_xS_2$ and electron-doped $Ni_{1-x}Cu_xS_2$ single crystals: (a) the weak ferromagnetic (WF) magnetization M_{wf}, (b) the low-T (2–5 K) coercive field H_c, (c) the 75-K magnitude of the zero-field-cooled/field-cooled (ZFC/FC) magnetization splitting, (d) the resistivity (ρ) at 20 K (left axis) and 300 K (right axis), (e) the bulk resistivity activation energy E_a, (f) the Sommerfeld coefficient γ (left axis) and the Debye temperature θ_D (right axis), and (g) the magnitude of the heat capacity C_p at the WF transition temperature T_{wf}. M_{wf} and H_c in (a) and (b) were obtained from Figs. 3(k)–3(o), M_{wf} being determined from zero-field extrapolations of linear fits to high-field $M(H)$ data. Data in (c) were obtained from Figs. 3(a)–3(e), with the down arrows signifying upper bounds as the measured values plotted are on the same order as the measurement resolution. Data in (d) were obtained from Fig. 6. E_a data in (e) were obtained from linear (i.e., Arrhenius or simple-activated) fits to $\log_{10}\rho$ vs T^{-1} plots from the high-T (150–300 K) bulk-dominated region in Fig. 6. Finally, γ, θ_D, and $C_p(T_{wf})$ data in (f) and (g) were obtained from the data shown in Fig. 4. Throughout the figure, blue refers to magnetometry data, red to transport data, and green to specific heat data.

D. Doping dependence summary

On the basis of the data depicted in Figs. 3–6, and connecting to Fig. 2, Fig. 7 summarizes the doping dependence of

key magnetic, electronic, and thermodynamic parameters of electron- and hole-doped NiS_2. Starting with magnetic properties, Fig. 7(a) reproduces $M_{wf}(x)$ from Fig. 2(b) for reference. As already noted, this reveals the electron/hole-asymmetric suppression of the WF magnetization with doping, because of the evolution in magnetic inhomogeneity depicted in Figs. 2(c)–2(f). As alluded to in the discussion of Figs. 3(k)–3(o), this is accompanied by nontrivial variations in the coercivity (H_c) associated with the WF order. The full $H_c(x)$ is shown in Fig. 7(b), which, in addition to the necessary vanishing at sufficiently high electron and hole doping (owing to suppression of WF order), also shows a sharp minimum at $x = 0$. We believe that two factors dominate this $H_c(x)$. First, as x is increased from zero in both $Ni_{1-x}Co_xS_2$ and $Ni_{1-x}Cu_xS_2$, the decrease in M_{wf} [Fig. 7(a)] must naturally drive an increase in H_c [Fig. 7(b)]. In the Stoner-Wohlfarth model of coherent magnetization rotation, for example, $H_c = 2K_u/M_s$, where K_u is the effective uniaxial magnetic anisotropy constant and M_s is the saturation magnetization [78]. A decreasing M_s with increasing x thus naturally increases H_c. Second, if domain effects are relevant, the Co and Cu doping will generate domain wall pinning sites [79], and eventually clusters [see Fig. 2(d)], which would hinder domain motion and thus also increase H_c. We believe that these factors lead to the initial increase in H_c with electron/hole doping, before the suppression of the WF order drives H_c to zero, leading to the form of $H_c(x)$ in Fig. 7(b). Electron/hole asymmetry is again apparent, in close accord with Fig. 7(a). Figure 7(c) complements these analyses, showing the magnitude of the FC/ZFC splitting at 75 K [see Fig. 3(a), for example], a parameter designed to track the high-T_{ND} AF order. As would be expected based on Figs. 2(c)–2(f), this is negligibly small at low doping [note the $\log_{10}$ scale in Fig. 7(c)] but then gradually rises with doping, out to $x = 0.20$ in the hole-doped case. The inverse correlation with Fig. 7(a) is clear, the WF order of the near-undoped regions in Figs. 2(c)–2(f) being gradually suppressed as the high-T_{ND} AF order of the doped regions is enhanced.

Figures 7(d) and 7(e) then turn to electronic transport. Figure 7(d) shows the 20-K resistivity (left axis, red-filled circles) and 300-K resistivity (right axis, red-open circles), representing the low-T and high-T (bulk-dominated) behaviors. Consistent with the discussion of Fig. 6, ρ(300 K) is clearly electron/hole asymmetric. Electron doping in $Ni_{1-x}Cu_xS_2$ initially rapidly decreases ρ(300 K), before a narrow plateau, then another weak decrease as the effective solubility limit of Cu is approached. Hole doping in $Ni_{1-x}Co_xS_2$, on the other hand, induces a more gradual decrease in ρ(300 K) out to $x = 0.20$ and beyond [Fig. 6(a)]. ρ(20 K) has a similar electron/hole doping dependence to ρ(300 K), albeit over a larger range, as would be expected. Figure 7(e) further reinforces these conclusions by plotting the doping dependence of the activation energy extracted from the high-T, bulk-dominated $\rho(T)$, where the correlations with Figs. 7(a) and 7(d) are striking.

Finally, Figs. 7(f) and 7(g) present thermodynamic quantities. Figure 7(f) (left axis) shows the full doping dependence of γ from the low-T $C_p(T)$. This is of course negligible in undoped Mott-insulating NiS_2, then rises asymmetrically for electron and hole doping. Most significantly, the onset of clearly nonzero γ occurs before the insulator-metal transitions (the vertical-dashed lines in Fig. 7), strongly supporting the electronic phase coexistence scenario depicted in Figs. 2(c)–2(f) [75,76]. Figure 7(f) (right axis) shows the corresponding doping dependence of the θ_D from the low-T $C_p(T)$ analysis [Figs. 4(k)–4(o)], which also rises asymmetrically for electron and hole doping. As already noted, the primary factor responsible for this behavior is likely the excess unit-cell volume shown in Fig. 1(e) (right axis), since the decreased cell volume with doping should naturally generate lattice stiffening and thus higher θ_D. Figure 7(g) then plots $C_p(T_{wf})$, i.e., the magnitude of the specific heat peak due to the onset of WF order. In accord with Fig. 7(a), this is large in NiS_2, where the AF/WF phase is dominant, but is diminished with doping as the Mott-insulating low-T_N AF/WF phase is suppressed in favor of the metallic high-T_{ND} AF phase.

E. Discussion and DMFT results

Together, the data of Figs. 1 and 3–6 paint a clear phenomenological picture of the transition from AF Mott insulator to AF metal in electron- and hole-doped NiS_2, as summarized in Figs. 2 and 7. First, both electron and hole doping indeed lead to rapid stabilization of high-T_{ND} metallic AF states, which saturate at the critical doping levels [Fig. 2(a)] [3,4,10]. As this takes place, the low-T_N Mott-insulating AF/WF phase is suppressed not by reduction of T_N and T_{wf} [see Fig. 2(a)], but instead by suppression of the magnetization associated with this order [Figs. 2(b) and 7(a)], strongly suggesting electronic and magnetic phase coexistence across a spatially inhomogeneous Mott insulator-metal transition. This is further supported by the emergence of a finite Sommerfeld coefficient even on the insulating side of the transition [Fig. 7(f)] [75,76], and the coexistence of AF ordering at T_{ND} and T_N [Fig. 5(e)]. Both electron- and hole-doped NiS_2 thus join a growing list of Mott insulators in which doping induces electronic and magnetic phase coexistence and strikingly inhomogeneous Mott transitions. This includes doped perovskite titanates such as $LaTiO_{3+\delta}$ [80] and $Y_{1-x}Ca_xTiO_3$ [81], cuprates such as $La_{2-x}Sr_xCuO_4$ [82], and iridates/ruthenates such as $Sr_3(Ir_{1-x}Ru_x)_2O_7$ [83]. This general behavior has been interpreted in terms of electronic phase coexistence of undoped (i.e., half-filled Mott-insulating) and doped (metallic) regions across a first-order Mott insulator-metal transition, as in several theoretical approaches [84,85]. In light of our findings, NiS_2 may be another system displaying such physics.

The Mott transition in doped NiS_2 is also found to be notably electron/hole asymmetric. The doping evolution of all key parameters in $Ni_{1-x}Co_xS_2$ is gradual, out to a critical doping level of $x \approx 0.125$ [Figs. 2(a), 2(b), and 7]. In $Ni_{1-x}Cu_xS_2$, on the other hand, the evolution with doping is more rapid, the critical doping level is only $x \approx 0.03$, and there is even evidence of two-stage character to the transition [see Figs. 2(a), 2(b), 7(a), 7(d), and 7(e) in particular]. Complementary DMFT results, shown in Fig. 8, provide significant insight into the origin of this doping asymmetry. Consistent with prior DFT + DMFT studies [86,87], a metallic state is found in DFT, but a gap of ~0.5 eV opens in DMFT. This is shown in Fig. 8(a), where the spectral function

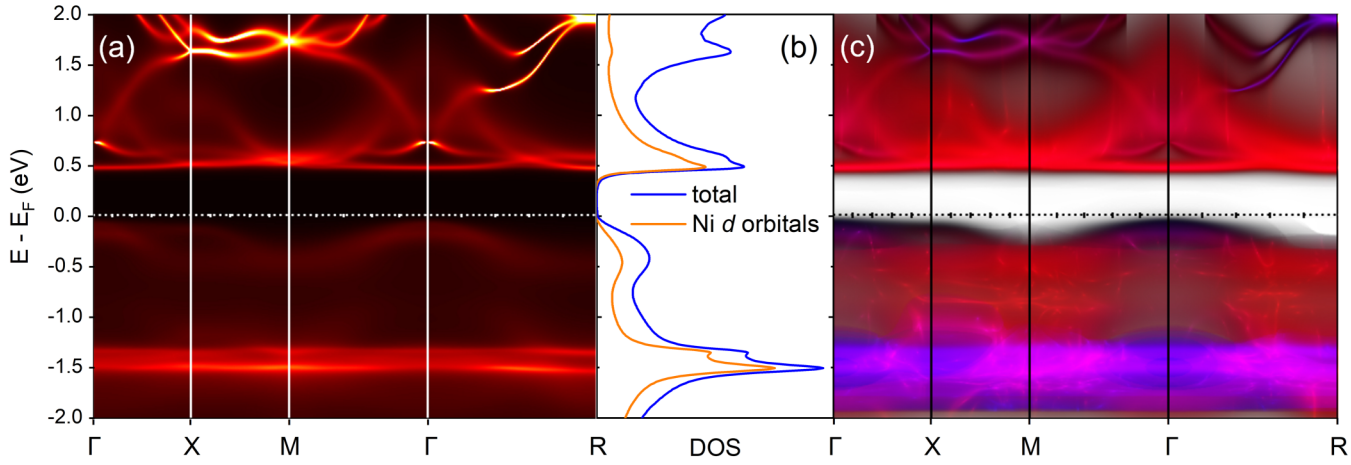

FIG. 8. (a) Total spectral function $A(k,\omega)$ of undoped NiS_2 from dynamical mean-field theory (DMFT) at 232 K. Energies are shown relative to the Fermi energy E_F. (b) Corresponding density-of-states (DOS) in arbitrary units, both total (blue line) and from Ni d orbitals alone (orange line). (c) Orbitally projected spectral function of undoped NiS_2, where red shades indicate Ni e_g states, blue shades indicate Ni t_{2g} states, and black indicates S weight. Γ, X, M, and R correspond to the k points (0,0,0), (0,1/2,0), (1/2,1/2,0), and (1/2,1/2,1/2).

is plotted. Interestingly, the corresponding density-of-states (DOS) in Fig. 8(b) reveals a far more complex situation than an isolated Ni e_g band split into upper and lower Hubbard bands [3,4,22,88]. The total DOS immediately above and below the gap does have substantial Ni d weight, but also significant contributions from S states. Most importantly in the current context, a striking feature in Fig. 8(a) is the far higher coherence (i.e., sharper features) just above the gap (the "conduction band") compared to just below the gap (the "valence band") [86,87], as also reflected in the magnitude of the DOS peaks in Fig. 8(b). Upon doping NiS_2, one would thus expect that a coherent, weakly correlated metallic state should be stabilized more rapidly with electron doping than hole doping, in qualitative agreement with our experimental observations such as those in Figs. 7(d) and 7(e). (While Hund's-coupling-induced correlations could affect this picture, Hund's metallicity has been discussed in NiS_2 only with Se substitution or under pressure, and is not predicted in carrier-doped NiS_2 [89,90]). The orbitally projected spectral function in Fig. 8(c) provides further insight into this by depicting the Ni t_{2g} states in blue shades, Ni e_g states in red shades, and S states in black. The region just above the gap ("conduction band") is seen to be composed of predominantly weakly correlated bands, likely S antibonding bands that attain e_g character through hybridization. The region just below the gap ("valence band"), on the other hand, has substantial S weight but is mixed with strongly correlated e_g states. These DMFT results thus provide a semiquantitative basis for the observed electron/hole doping asymmetry in NiS_2.

Finally, it is instructive to attempt to connect our findings regarding electronic and magnetic behavior with the structural data of Figs. 1(e) and 1(f) and Fig. S2 within the SM [71]. The first point to make here is that the asymmetric evolution of the excess unit cell volume with doping [Fig. 1(e), right axis] bears obvious and striking similarity to the electronic and magnetic evolutions in, for example, Figs. 7(a), 7(b), 7(d), and 7(e). Clearly, the excess cell volume in doped NiS_2 can be definitively associated with the Mott-insulating AF/WF phase. As this Mott-insulating phase is suppressed by doping, in an electron/hole-asymmetric fashion [consider the bulk-dominated ρ(300 K) on the right axis of Fig. 7(d)], the cell volume collapses to the expected level [Fig. 1(e), right axis]. Future theoretical work is clearly needed to further explore this connection between cell volume and relative electronic correlation strength in doped/substituted NiS_2. Similarly, the $T_{ND}(x)$ behavior in Fig. 2(a) needs further theoretical consideration. An early study by Ogawa and coworkers [3] emphasized the interconnections between $T_{ND}(x)$, $\Delta a(x)$, and $E_a(x)$, arguing that T_{ND} should be maximized at the Mott-Hubbard transition as Δa and E_a vanish [3]; this was based heavily on the Hubbard model theoretical study of Plische [91] and Kubo [92]. Considering Figs. 1(f) and S2 within the SM [71], it is also clear that the broad maximum in the XRD peak widths in $Ni_{1-x}Co_xS_2$ overlaps with the critical doping level for the Mott transition. This strongly suggests that the electronic/magnetic inhomogeneity that results from the coexistence of regions with near-undoped T_N and T_{wf} with regions with high T_{ND} is accompanied by structural/chemical inhomogeneity, as well as potential local symmetry breaking. This is very likely tied to the behavior in Fig. 1(e), i.e., the regions with near-undoped electronic/magnetic properties will have substantially expanded cell volumes while the heavily doped regions will have cell volumes in-line with the Vegard law prediction. This is another factor that has not yet been highlighted in the literature on $Ni_{1-x}Co_xS_2$, $Ni_{1-x}Cu_xS_2$, $NiS_{2-x}Se_x$, pressurized NiS_2, etc., emphasizing the strong coupling of structural, chemical, electronic, and magnetic degrees of freedom in this system.

IV. SUMMARY

We have presented a detailed study of the structural, magnetic, electronic, and thermodynamic properties of $Ni_{1-x}Co_xS_2$ and $Ni_{1-x}Cu_xS_2$ single crystals, spanning the critical regions for the transitions from Mott insulator to metal. A revised electronic phase diagram has thus been generated, significantly modifying the understanding of the electronic and magnetic properties across the Mott insulator-metal transition

in this model highly correlated system. The rapid stabilization of a high-T_{ND} metallic AF state with doping is confirmed, but along with the persistent observation of the T_N and T_{wf} of the undoped parent phase. This low-T_N Mott-insulating AF/WF phase is suppressed not through the decrease of T_N and T_{wf}, but instead by the decrease of the magnetization of this phase, strongly implicating electronic/magnetic phase coexistence across a spatially inhomogeneous Mott transition. This is further supported by numerous features of the detailed doping dependencies of the electronic, magnetic, and thermodynamic parameters in this system. The Mott insulator-metal transition in doped NiS_2 is also found to be electron/hole asymmetric, and is accompanied by clear structural anomalies and inhomogeneity, providing yet deeper insight into the physics of this system. These results significantly revise and improve the understanding of the transition from AF Mott insulator to AF metal in electron- and hole-doped NiS_2, highlighting a number of issues that clearly require further theoretical attention. Through such studies, we hope that a complete understanding of the insulator-metal transition in this model Mott insulator can finally be obtained.

Note added. Recently, the authors became aware of Yasui *et al.* [93]. In that work it is suggested that the surface conduction in NiS_2 single crystals arises not at the entire surface but instead at surface step edges. This does not alter the claims in the current paper regarding surface vs bulk conduction, instead refining the nature and location of the surface conducting states.

All data in this paper are available at DRUM (the Data Repository for the University of Minnesota) [94].

ACKNOWLEDGMENTS

This work was primarily supported by the Department of Energy through the University of Minnesota (UMN) Center for Quantum Materials under Grant No. DE-SC0016371. A portion of this research used resources at the High Flux Isotope Reactor, a DOE Office of Science User Facility operated by the Oak Ridge National Laboratory. The beam time was allocated to HB-2A on Proposal No. IPTS-32045.1. Y.L.'s contribution was supported by the Minnesota Environment and Natural Resources Trust Fund (ENRTF), as recommended by the Legislative-Citizen Commission on Minnesota Resources (LCCMR). Parts of this work were conducted in the UMN Characterization Facility, which is also partially supported by the National Science Foundation through the MRSEC Program under Grant No. DMR-2011401.

[1] H. S. Jarrett, W. H. Cloud, R. J. Bouchard, S. R. Butler, C. G. Frederick, and J. L. Gillson, Evidence for itinerant *d*-electron ferromagnetism, Phys. Rev. Lett. **21**, 617 (1968).

[2] T. A. Bither, R. J. Bouchard, W. H. Cloud, P. C. Donohue, and W. J. Siemons, Transition metal pyrite dichalcogenides. high-pressure synthesis and correlation of properties, Inorg. Chem. **7**, 2208 (1968).

[3] S. Ogawa, S. Waki, and T. Teranishi, Magnetic and electrical properties of 3D transition-metal disulfides having the pyrite structure, Int. J. Magn. **5**, 349 (1974).

[4] S. Ogawa, Magnetic properties of 3D transition-metal dichalcogenides with the pyrite structure, J. Appl. Phys. **50**, 2308 (1979).

[5] L. Wang, T. Y. Chen, and C. Leighton, Spin-dependent band structure effects and measurement of the spin polarization in the candidate half-metal CoS_2, Phys. Rev. B **69**, 094412 (2004).

[6] L. Wang, K. Umemoto, R. M. Wentzcovitch, T. Y. Chen, C. L. Chien, J. G. Checkelsky, J. C. Eckert, E. D. Dahlberg, and C. Leighton, $Co_{1-x}Fe_xS_2$: A tunable source of highly spin-polarized electrons, Phys. Rev. Lett. **94**, 056602 (2005).

[7] L. Wang, T. Y. Chen, C. L. Chien, J. G. Checkelsky, J. C. Eckert, E. D. Dahlberg, K. Umemoto, R. M. Wentzcovitch, and C. Leighton, Composition controlled spin polarization in $Co_{1-x}Fe_xS_2$: Electronic, magnetic, and thermodynamic properties, Phys. Rev. B **73**, 144402 (2006).

[8] C. Leighton, M. Manno, A. Cady, J. W. Freeland, L. Wang, K. Umemoto, R. M. Wentzcovitch, T. Y. Chen, C. L. Chien, P. L. Kuhns *et al.*, Composition controlled spin polarization in $Co_{1-x}Fe_xS_2$ alloys, J. Phys.: Condens. Matter **19**, 315219 (2007).

[9] K. Ramesha, R. Seshadri, C. Ederer, T. He, and M. A. Subramanian, Experimental and computational investigation of structure and magnetism in pyrite $Co_{1-x}Fe_xS_2$: Chemical bonding and half-metallicity, Phys. Rev. B **70**, 214409 (2004).

[10] S. Ogawa, Specific heat study of magnetic ordering and band structure of 3D transition metal disulfides having the pyrite structure, J. Phys. Soc. Jpn. **41**, 462 (1976).

[11] T. A. Bither, P. C. Donohue, W. H. Cloud, P. E. Bierstedt, and H. S. Young, Mixed-cation transition metal pyrite dichalcogenides—High pressure synthesis and properties, J. Solid State Chem. **1**, 526 (1970).

[12] A. K. Mabatah, E. J. Yoffa, P. C. Eklund, M. S. Dresselhaus, and D. Adler, Anomalous electrical transport properties of $Ni_{1-x}Co_xS_2$, Phys. Rev. Lett. **39**, 494 (1977).

[13] A. K. Mabatah, E. J. Yoffa, P. C. Eklund, M. S. Dresselhaus, and D. Adler, Electrical properties of $Ni_{1-x}Co_xS_2$, Phys. Rev. B **21**, 1676 (1980).

[14] P. Kwizera, A. K. Mabatah, M. S. Dresselhaus, and D. Adler, Electrical properties of $Ni_{1-z}Cu_zS_2$, Phys. Rev. B **24**, 2972 (1981).

[15] A. Maignan, R. Daou, E. Guilmeau, D. Berthebaud, T. Barbier, O. Lebedev, and S. Hébert, Thermoelectric properties, metal-insulator transition, and magnetism: Revisiting the $Ni_{1-x}Cu_xS_2$ system, Phys. Rev. Mater. **3**, 115401 (2019).

[16] G. Krill, M. F. Lapierre, C. Robert, F. Gautier, G. Czjzek, J. Fink, and H. Schmidt, Electronic and magnetic properties of the pyrite-structure compound NiS_2: Influence of vacancies and copper impurities, J. Phys. C: Solid State Phys. **9**, 761 (1976).

[17] H. Betsuyaku, Y. Hamaguchi, and S. Ogawa, Neutron diffraction study of $Ni_{0.9}Cu_{0.1}S_2$, J. Phys. Soc. Jpn. **37**, 983 (1974).

[18] Y. Nishihara, S. Ogawa, and S. Waki, Mössbauer study of $Ni^{57}_{0.995}Fe_{0.005}S_2$ − magnetic structure of NiS_2−, J. Phys. Soc. Jpn. **39**, 63 (1975).

[19] F. Gautier, G. Krill, M. F. Lapierre, P. Panissod, C. Robert, G. Czjzek, J. Fink, and H. Schmidt, Existence of an antiferromagnetic metallic phase (AFM) in the $NiS_{2-x}Se_x$ system with pyrite structure, Phys. Lett. A **53**, 31 (1975).

[20] P. Kwizera, M. S. Dresselhaus, and D. Adler, Electrical properties of $NiS_{2-x}Se_x$, Phys. Rev. B **21**, 2328 (1980).

[21] Y. Sekine, H. Takahashi, N. Môri, T. Matsumoto, and T. Kosaka, Effect of pressure on transport properties of $Ni(S_{1-x}Se_x)_2$, Physica B: Condens. Matter **237–238**, 148 (1997).

[22] J. M. Honig and J. Spałek, Electronic properties of $NiS_{2-x}Se_x$ single crystals: From magnetic Mott−Hubbard insulators to normal metals, Chem. Mater. **10**, 2910 (1998).

[23] S. Yano, D. Louca, J. Yang, U. Chatterjee, D. E. Bugaris, D. Y. Chung, L. Peng, M. Grayson, and M. G. Kanatzidis, Magnetic structure of $NiS_{2-x}Se_x$, Phys. Rev. B **93**, 024409 (2016).

[24] M. Matsuura, H. Hiraka, K. Yamada, and Y. Endoh, Magnetic phase diagram and metal-insulator transition of $NiS_{2-x}Se_x$, J. Phys. Soc. Jpn. **69**, 1503 (2000).

[25] S. Miyasaka, H. Takagi, Y. Sekine, H. Takahashi, N. Môri, and R. J. Cava, Metal-insulator transition and itinerant antiferromagnetism in $NiS_{2-x}Se_x$ pyrite, J. Phys. Soc. Jpn. **69**, 3166 (2000).

[26] X. Yao, J. M. Honig, T. Hogan, C. Kannewurf, and J. Spałek, Electrical properties of $NiS_{2-x}Se_x$ single crystals: From Mott insulator to paramagnetic metal, Phys. Rev. B **54**, 17469 (1996).

[27] T. A. Bither, C. T. Prewitt, J. L. Gillson, P. E. Bierstedt, R. B. Flippen, and H. S. Young, New transition metal dichalcogenides formed at high pressure, Solid State Commun. **4**, 533 (1966).

[28] S. El-Khatib, B. Voigt, B. Das, A. Stahl, W. Moore, M. Maiti, and C. Leighton, Conduction via surface states in antiferromagnetic Mott-insulating NiS_2 single crystals, Phys. Rev. Mater. **5**, 115003 (2021).

[29] S. El-Khatib, F. Mustafa, M. Egilmez, B. Das, Y. Tao, M. Maiti, Y. Lee, and C. Leighton, Exotic surface magnetotransport phenomena in the antiferromagnetic Mott insulator NiS_2, Phys. Rev. Mater. **7**, 104401 (2023).

[30] T. Thio and J. W. Bennett, Hall effect and conductivity in pyrite NiS_2, Phys. Rev. B **50**, 10574 (1994).

[31] D. D. Sarma *et al.*, Metal-insulator crossover behavior at the surface of NiS_2, Phys. Rev. B **67**, 155112 (2003).

[32] R. Hartmann *et al.*, Intrinsic giant magnetoresistance due to exchange-bias-type effects at the surface of single-crystalline NiS_2 nanoflakes, Nanoscale **15**, 10277 (2023).

[33] K. D. M. Rao, T. Bhuvana, B. Radha, N. Kurra, N. S. Vidhyadhiraja, and G. U. Kulkarni, Metallic conduction in NiS_2 nanocrystalline structures, J. Phys. Chem. C **115**, 10462 (2011).

[34] M. Limpinsel, N. Farhi, N. Berry, J. Lindemuth, C. L. Perkins, Q. Lin, and M. Law, An inversion layer at the surface of *n*-type iron pyrite, Energy Environ. Sci. **7**, 1974 (2014).

[35] J. Walter, X. Zhang, B. Voigt, R. Hool, M. Manno, F. Mork, E. S. Aydil, and C. Leighton, Surface conduction in *n* -type pyrite FeS_2 single crystals, Phys. Rev. Mater. **1**, 065403 (2017).

[36] D. Liang, M. Cabán-Acevedo, N. S. Kaiser, and S. Jin, Gated hall effect of nanoplate devices reveals surface-state-induced surface inversion in iron pyrite semiconductor, Nano Lett. **14**, 6754 (2014).

[37] B. Voigt, W. Moore, M. Manno, J. Walter, J. D. Jeremiason, E. S. Aydil, and C. Leighton, Transport evidence for sulfur vacancies as the origin of unintentional *n*-type doping in pyrite FeS_2, ACS Appl. Mater. Interfaces **11**, 15552 (2019).

[38] B. Voigt, W. Moore, M. Maiti, J. Walter, B. Das, M. Manno, C. Leighton, and E. S. Aydil, Observation of an internal *p–n* junction in pyrite FeS_2 single crystals: Potential origin of the low open circuit voltage in pyrite solar cells, ACS Mater. Lett. **2**, 861 (2020).

[39] M. Cabán-Acevedo, N. S. Kaiser, C. R. English, D. Liang, B. J. Thompson, H.-E. Chen, K. J. Czech, J. C. Wright, R. J. Hamers, and S. Jin, Ionization of high-density deep donor defect states explains the low photovoltage of iron pyrite single crystals, J. Am. Chem. Soc. **136**, 17163 (2014).

[40] B. Voigt, B. Das, D. M. Carr, D. Ray, M. Maiti, W. Moore, M. Manno, J. Walter, E. S. Aydil, and C. Leighton, Mitigation of the internal *p-n* junction in CoS_2-contacted FeS_2 single crystals: Accessing bulk semiconducting transport, Phys. Rev. Mater. **5**, 025405 (2021).

[41] B. Voigt, L. S. Valor, W. Moore, J. Jeremiason, J. Kakalios, E. S. Aydil, and C. Leighton, Controlled *p*-type doping of pyrite FeS_2, ACS Appl. Mater. Interfaces **15**, 28258 (2023).

[42] J. Walter, B. Voigt, E. Day-Roberts, K. Heltemes, R. M. Fernandes, T. Birol, and C. Leighton, Voltage-induced ferromagnetism in a diamagnet, Sci. Adv. **6**, eabb7721 (2020).

[43] D. Ray, B. Voigt, M. Manno, C. Leighton, E. S. Aydil, and L. Gagliardi, Sulfur vacancy clustering and its impact on electronic properties in pyrite FeS_2, Chem. Mater. **32**, 4820 (2020).

[44] N. Wu, R. F. Sabirianov, W. N. Mei, Y. B. Losovyj, N. Lozova, M. Manno, C. Leighton, and P. A. Dowben, The minority spin surface bands of $CoS_2(001)$, J. Phys.: Condens. Matter **21**, 295501 (2009).

[45] R. L. Kautz, M. S. Dresselhaus, D. Adler, and A. Linz, Electrical and optical properties of NiS_2, Phys. Rev. B **6**, 2078 (1972).

[46] T. Miyadai, K. Takizawa, H. Nagata, H. Ito, S. Miyahara, and K. Hirakawa, Neutron diffraction study of NiS_2 with pyrite structure, J. Phys. Soc. Jpn. **38**, 115 (1975).

[47] K. Kikuchi, Magnetic study of NiS_2 single crystals, J. Phys. Soc. Jpn. **47**, 484 (1979).

[48] M. Matsuura, Y. Endoh, H. Hiraka, K. Yamada, A. S. Mishchenko, N. Nagaosa, and I. V. Solovyev, Classical and quantum spin dynamics in the fcc antiferromagnet NiS_2 with frustration, Phys. Rev. B **68**, 094409 (2003).

[49] P. G. Niklowitz, P. L. Alireza, M. J. Steiner, G. G. Lonzarich, D. Braithwaite, G. Knebel, J. Flouquet, and J. A. Wilson, Unconventional resistivity at the border of metallic antiferromagnetism in NiS_2, Phys. Rev. B **77**, 115135 (2008).

[50] Y. Feng, R. Jaramillo, A. Banerjee, J. M. Honig, and T. F. Rosenbaum, Magnetism, structure, and charge correlation at a pressure-induced Mott-Hubbard insulator-metal transition, Phys. Rev. B **83**, 035106 (2011).

[51] T. Higo and S. Nakatsuji, Magnetization anomaly due to the non-coplanar spin structure in NiS_2, J. Phys. Soc. Jpn. **84**, 053702 (2015).

[52] C. Clark and S. Friedemann, Atomic diffusion in the surface state of Mott insulator NiS_2, J. Magn. Magn. Mater. **400**, 56 (2016).

[53] M. Matsuura, H. Hiraka, Y. Endoh, K. Hirota, and K. Yamada, Direct evidence of spin frustration in the fcc antiferromagnet NiS_2, Appl. Phys. A: Mater. **74**, s792 (2002).

[54] K. Kikuchi, T. Miyadai, T. Fukui, H. Itô, and K. Takizawa, Spin structure and magnetic properties of NiS_2, J. Phys. Soc. Jpn. **44**, 410 (1978).

[55] J. M. Hastings and L. M. Corliss, Ordered moment of NiS_2, IBM J. Res. & Dev. **14**, 227 (1970).

[56] T. Thio, J. W. Bennett, and T. R. Thurston, Surface and bulk magnetic properties of pyrite NiS_2: Magnetization and neutron-scattering studies, Phys. Rev. B **52**, 3555 (1995).

[57] H. Nagata, H. Ito, and T. Miyadai, Thermal expansion and crystal distortion of NiS_2, J. Phys. Soc. Jpn. **41**, 2133 (1976).

[58] S. Hameed *et al.*, Electrochemical mechanism of ionic-liquid gating in antiferromagnetic Mott-insulating NiS_2 single crystals, Phys. Rev. Mater. **6**, 064601 (2022).

[59] L. Wang, T. Y. Chen, C. L. Chien, and C. Leighton, Sulfur stoichiometry effects in highly spin polarized CoS_2 single crystals, Appl. Phys. Lett. **88**, 232509 (2006).

[60] JADE 9.1; Materials Data: Livermore, CA (2019), https://www.icdd.com/mdi-jade/.

[61] J. C. Lashley *et al.*, Critical examination of heat capacity measurements made on a quantum design physical property measurement system, Cryogenics **43**, 369 (2003).

[62] B. H. Toby and R. B. Von Dreele, GSAS-II: The genesis of a modern open-source all purpose crystallography software package, J. Appl. Crystallogr. **46**, 544 (2013).

[63] K. Haule, C.-H. Yee, and K. Kim, Dynamical mean-field theory within the full-potential methods: Electronic structure of $CeIrIn_5$, $CeCoIn_5$, and $CeRhIn_5$, Phys. Rev. B **81**, 195107 (2010).

[64] K. Haule, Structural predictions for correlated electron materials using the functional dynamical mean field theory approach, J. Phys. Soc. Jpn. **87**, 041005 (2018).

[65] P. Blaha, K. Schwarz, F. Tran, R. Laskowski, G. K. H. Madsen, and L. D. Marks, WIEN2k: An APW+lo program for calculating the properties of solids, J. Chem. Phys. **152**, 074101 (2020).

[66] K. Haule, Exact double counting in combining the dynamical mean field theory and the density functional theory, Phys. Rev. Lett. **115**, 196403 (2015).

[67] H. Shinaoka, J. Otsuki, M. Ohzeki, and K. Yoshimi, Compressing Green's function using intermediate representation between imaginary-time and real-frequency domains, Phys. Rev. B **96**, 035147 (2017).

[68] K. Haule, T. Birol, and G. Kotliar, Covalency in transition-metal oxides within all-electron dynamical mean-field theory, Phys. Rev. B **90**, 075136 (2014).

[69] S. Mandal, K. Haule, K. M. Rabe, and D. Vanderbilt, Systematic beyond-DFT study of binary transition metal oxides, npj Comput. Mater. **5**, 115 (2019).

[70] T. Fujii, K. Tanaka, F. Marumo, and Y. Noda, Structural behaviour of NiS_2 up to 54 kbar, Mineral. J. **13**, 448 (1987).

[71] See Supplemental Material at http://link.aps.org/supplemental/10.1103/PhysRevMaterials.8.114420 for additional EDS data on $Ni_{1-x}Co_xS_2$ and $Ni_{1-x}Cu_xS_2$ single crystals, microstrain analysis using powder x-ray diffraction data collected on ground single crystals of $Ni_{1-x}Co_xS_2$ and $Ni_{1-x}Cu_xS_2$, effect of various structural, magnetic, and transport parameters on the S:Ni loading in the NiS_2 crystal growth tube, and a comparison of the temperature dependence of the electrical resistivity and its derivative of $Ni_{1-x}Co_xS_2$ and $Ni_{1-x}Cu_xS_2$ single crystals with literature.

[72] C. Kittel, *Introduction to Solid State Physics*, 8th Ed. (John Wiley & Sons, New York, 2005).

[73] E. S. R. Gopal, *Specific Heats at Low Temperatures* (Springer, New York, 1966).

[74] H. M. Rosenberg, *Low Temperature Solid State Physics* (Oxford University Press, New York, 1963).

[75] C. He, S. Eisenberg, C. Jan, H. Zheng, J. F. Mitchell, and C. Leighton, Heat capacity study of magnetoelectronic phase separation in $La_{1-x}Sr_xCoO_3$ single crystals, Phys. Rev. B **80**, 214411 (2009).

[76] C. He, S. El-Khatib, J. Wu, J. W. Lynn, H. Zheng, J. F. Mitchell, and C. Leighton, Doping fluctuation-driven magneto-electronic phase separation in $La_{1-x}Sr_xCoO_3$ single crystals, EPL **87**, 27006 (2009).

[77] S. Hameed *et al.*, Nature of the ferromagnetic-antiferromagnetic transition in $Y_{1-x}La_xTiO_3$, Phys. Rev. B **104**, 024410 (2021).

[78] R. C. O'Handley, *Modern Magnetic Materials Principles and Applications* (John Wiley & Sons, New York, 2000).

[79] H. Kronmüller, *Micromagnetism and the Microstructure of Ferromagnetic Solids*, 1st Ed. (Cambridge University Press, Cambridge, 2003).

[80] H. D. Zhou and J. B. Goodenough, Coexistence of two electronic phases in $LaTiO_{3+\delta}$($0.01 \leqslant \delta \leqslant 0.12$) and their evolution with δ, Phys. Rev. B **71**, 165119 (2005).

[81] S. Hameed, J. Joe, D. M. Gautreau, J. W. Freeland, T. Birol, and M. Greven, Two-component electronic phase separation in the doped Mott insulator $Y_{1-x}Ca_xTiO_3$, Phys. Rev. B **104**, 045112 (2021).

[82] R. S. Markiewicz, Phase separation near the Mott transition in $La_{2-x}Sr_xCuO_4$, J. Phys.: Condens. Matter **2**, 665 (1990).

[83] C. Dhital *et al.*, Carrier localization and electronic phase separation in a doped spin-orbit-driven Mott phase in $Sr_3(Ir_{1-x}Ru_x)_2O_7$, Nat. Commun. **5**, 3377 (2014).

[84] C.-H. Yee and L. Balents, Phase separation in doped Mott insulators, Phys. Rev. X **5**, 021007 (2015).

[85] J. M. Kurdestany and S. Satpathy, Mott metal-insulator transition in the doped Hubbard-Holstein model, Phys. Rev. B **96**, 085132 (2017).

[86] E. Day-Roberts, R. M. Fernandes, and T. Birol, Gating-induced Mott transition in NiS_2, Phys. Rev. B **107**, 085150 (2023).

[87] C.-Y. Moon, H. Kang, B. G. Jang, and J. H. Shim, Composition and temperature dependent electronic structures of $NiS_{2-x}Se_x$ alloys: First-principles dynamical mean-field theory approach, Phys. Rev. B **92**, 235130 (2015).

[88] J. B. Goodenough, Conceptual phase diagram and its application to the spontaneous magnetism of several pyrites, J. Solid State Chem. **3**, 26 (1971).

[89] B. G. Jang *et al.*, Direct observation of kink evolution due to Hund's coupling on approach to metal-insulator transition in $NiS_{2-x}Se_x$, Nat. Commun. **12**, 1208 (2021).

[90] I. Park, B. G. Jang, D. W. Kim, J. H. Shim, and G. Kotliar, Clean realization of Hund's physics near the mott transition: NiS_2 under pressure, Phys. Rev. B **109**, 045146 (2024).

[91] M. Plischke, Antiferromagnetic phase of the Hubbard model, Solid State Commun. **13**, 393 (1973).

[92] K. Kubo, The effect of electron correlation on the volume of a solid solution, J. Phys. Soc. Jpn. **42**, 529 (1977).

[93] Y. Yasui, K. Iwata, S. Okazaki, S. Miyasaka, Y. Sugimoto, T. Hanaguri, H. Takagi, and T. Sasagawa, Closing of the Mott gap near step edges in NiS_2, Phys. Rev. B **110**, 045139 (2024).

[94] https://doi.org/10.13020/mvgf-qh78.